

Star Formation Laws: the Effects of Gas Cloud Sampling

D. Calzetti¹, G. Liu^{1,2}, J. Koda³

ABSTRACT

Recent observational results indicate that the functional shape of the spatially-resolved star formation–molecular gas density relation depends on the spatial scale considered. These results may indicate a fundamental role of sampling effects on scales that are typically only a few times larger than those of the largest molecular clouds. To investigate the impact of this effect, we construct simple models for the distribution of molecular clouds in a typical star-forming spiral galaxy, and, assuming a power-law relation between SFR and cloud mass, explore a range of input parameters. We confirm that the slope and the scatter of the simulated SFR-molecular gas surface density relation depend on the size of the sub-galactic region considered, due to stochastic sampling of the molecular cloud mass function, and the effect is larger for steeper relations between SFR and molecular gas. There is a general trend for all slope values to tend to \sim unity for region sizes larger than 1–2 kpc, irrespective of the input SFR–cloud relation. The region size of 1–2 kpc corresponds to the area where the cloud mass function becomes fully sampled. We quantify the effects of selection biases in data tracing the SFR, either as thresholds (i.e., clouds smaller than a given mass value do not form stars) or backgrounds (e.g., diffuse emission unrelated to current star formation is counted towards the SFR). Apparently discordant observational results are brought into agreement via this simple model, and the comparison of our simulations with data for a few galaxies supports a steep (>1) power law index between SFR and molecular gas.

Subject headings: galaxies: ISM – ISM: structure – stars: formation

¹Dept. of Astronomy, University of Massachusetts, Amherst, MA 01003; calzetti@astro.umass.edu

²Dept. of Physics and Astronomy, The Johns Hopkins University, Baltimore, MD

³Dept. of Physics and Astronomy, State University of New York at Stony Brook, New York, NY

1. Introduction

The relation that links star formation to its gas reservoir is at the foundation of the evolution of the baryonic component of galaxies across cosmic times. Hence, large efforts have been expended in trying to determine whether such a relation obeys some universal scaling that may, in turn, clue to its physical underpinning.

Observational investigations of such relations in extragalactic environments were kick-started by a few influential works (e.g. Kennicutt 1989, 1998), and have continued for over two decades. Major progress in the sensitivity and angular resolution of infrared imaging data have enabled a better handling of the dust attenuation in star formation rate indicators (SFRs), while increased sensitivity and mapping speed have started to yield better radio maps tracing the gas components of galaxies. These important advances have enabled the investigation of external galaxies on kpc or sub-kpc scales, and this new capability has brought new challenges.

Evolving from the original work of Schmidt (1959), the relation between gas and star formation is often expressed as a power law:

$$\Sigma_{SFR}/(M_{\odot} \text{ yr}^{-1} \text{ kpc}^{-2}) \propto [\Sigma_{gas}/(M_{\odot} \text{ pc}^{-2})]^{\gamma}, \quad (1)$$

where Σ refers to the surface density of SFR and gas, and the value of γ should be related to the main physical mechanisms that originate the relation itself (e.g., Schmidt 1959; Madore 1977; Elmegreen 1989; Kennicutt 1989, 1998; Tan 2000; Krumholz & McKee 2005). The above equation and its variations are now customarily referred to as the Schmidt–Kennicutt Law (SK Law henceforth).

Spatially-resolved investigations have established that the atomic (HI) gas component is usually not closely associated with regions of current star formation, but the denser molecular clouds, traced by CO, are (Wong & Blitz 2002; Kennicutt et al. 2007). While there are valid considerations for including both atomic and molecular gas components when investigating the processes of star formation (Boissier et al. 2003), we will limit the analysis in this paper to the SFR–molecular gas relation. Even when analyzing the direct relation between SFR and the molecular gas component, there are substantial differences among the results reported by several authors that warrant further analysis.

To maintain clarity throughout this paper, we will term ‘Observed SK Law’ the power law relation:

$$\Sigma_{SFR}/(M_{\odot} \text{ yr}^{-1} \text{ kpc}^{-2}) \propto [\Sigma_{H_2}/(M_{\odot} \text{ pc}^{-2})]^{\gamma_{H_2}}, \quad (2)$$

between the SFR and the molecular gas surface densities. The formal error about the best fit slope γ_{H_2} is generally a poor representation of the dispersion of the observational

data about the best fit relation: the dispersion of the data is usually much larger than the uncertainty on γ_{H2} . It has become more and more common to report such dispersion as a separate measure; here we will term σ_{H2} the r.m.s. scatter of the data (either observational or simulation-produced) about the best fit relation, along the Σ_{SFR} axis in the log-log plot of equation 2.

Azimuthally-averaged radial profiles of SFR and gas surface densities for a number of nearby galaxies have yielded values of γ_{H2} in the range 0.8–2.2, depending on the galaxy, the extinction corrections applied to the SFRs, and other characteristics of the galaxies or the data (Wong & Blitz 2002; Boissier et al. 2003; Heyer et al. 2004; Verley et al. 2010), although the steeper values, $\gamma_{H2} \gtrsim 1.2$ –1.4, tend to be more common.

Spatially-resolved studies, where galaxy regions are divided into bins with sizes in the range ~ 180 –2,000 pc, have yielded $\gamma_{H2} \sim 0.7$ –1.9 (Rownd & Young 1999; Kennicutt et al. 2007; Thilker et al. 2007; Bigiel et al. 2008; Blanc et al. 2009; Verley et al. 2010; Onodera et al. 2010; Momose et al. 2010; Liu et al. 2011; Rahman et al. 2011). Discrepant results, however, have been obtained even when using the same data on the same galaxy: in M51a, Kennicutt et al. (2007) and Bigiel et al. (2008) derive $\gamma_{H2} \sim 1.37$ and 0.84, respectively. This discrepancy can be resolved when accounting for the different treatment of the SFR data by the two papers: while Kennicutt et al. (2007) remove the diffuse, low frequency emission from those data, Bigiel et al. (2008) do not. Liu et al. (2011) show that, after removal of the diffuse emission, γ_{H2} is a monotonically decreasing function of the spatial scale sampled in the two galaxies M51a and NGC3521. Liu et al. (2011) argue that the diffuse emission may be unrelated to current star formation. The exact values of γ_{H2} depend on the fitting method and the dynamical range and level of significance of the data included in the fits (Blanc et al. 2009; Verley et al. 2010; Onodera et al. 2010). The exponent of the Observed SK Law can be as large as ~ 1.9 –2.7 when measured in molecular clouds in the Milky Way over $\gtrsim 1$ kpc scales (Gutermuth et al. 2011). This large variation may hint at a more fundamental relation of the denser components of the molecular gas with the SFR, which often correlate linearly ($\gamma_{dense} \approx 1$, Gao & Solomon 2004; Lada, Lombardi & Alves 2010, and references therein). The value of the power law index connecting the SFR surface density to the gas surface density may itself be a function of the type of gas tracer employed: high density tracers (e.g., HCN) will yield $\gamma \approx 1$, while low density tracers (e.g., $^{12}\text{CO}(1-0)$) may be more likely to give $\gamma > 1$ (Narayanan et al. 2008; Juneau et al. 2009).

The large range displayed by observational measures of γ_{H2} has prevented so far the pinning down of the underlying mechanism that drives star formation. While an exponent $\gamma_{H2}=1.5$ belies the dominance of gravitational instability as the main mechanism for star formation for constant galaxy gas scaleheight, other models predict lower ($\gamma_{H2}=1$) or higher

($\gamma_{H2}=2$) exponents (e.g., Schmidt 1959; Scoville, Sanders, & Clemens 1986; Wyse & Silk 1989; Elmegreen 1989, 1994; Silk 1997; Kennicutt 1998; Tan 2000, 2010; Wong & Blitz 2002; Krumholz & McKee 2005), which are still within the range of observed values. Understanding the origin of the wide range of γ_{H2} values found in the literature will provide fundamental guidance to models of gas-to-star conversion (e.g. Elmegreen 2002; Mac Low & Klessen 2004; Krumholz et al. 2009; Monaco et al. 2011; Dobbs, Burkert & Pringle 2011).

Similarly important for understanding star formation, the spatial scale at which the Observed SK Law is no longer recovered would indicate the transition into a regime where the feedback from star formation or the differential motions between stars and gas become an important source of scatter. Kennicutt et al. (2007) and Thilker et al. (2007) noted that the scatter σ_{H2} of the data about the best fit relation in the Σ_{SFR} – Σ_{H2} plane decreases when the spatial scale sampled increases from ~ 400 – 500 pc to 1 – 2 kpc. Onodera et al. (2010) and Momose et al. (2010) indicate break-down scales of 80 pc and 250 pc for M33 and NGC4303, respectively. Momose et al. (2010) recovers a SK Law on scales no smaller than ~ 1 kpc. Finally, Liu et al. (2011) reports that σ_{H2} is a monotonically decreasing function of the spatial sampling scale, between ~ 200 pc and ≈ 1 kpc, in M51a and NGC3521. Feldmann, Gnedin & Kravtsov (2011) have investigated the impact of environmental parameters, such as the UV radiation field or the shielding offered by the presence of metals as a reason for a smooth trend of σ_{H2} with spatial scale.

The main difficulty of most spatially resolved investigations is to disentangle effects due to the underlying physical mechanisms from those of statistical variations due to the sampling and fitting procedures. Here we employ Monte Carlo simulations to explore the impact on both γ_{H2} and σ_{H2} of the sampling region’s size as affected by the stochastic sampling of molecular clouds within the region, and other geometrical factors. We will also investigate the impact of the fitting procedure and of the data dynamical range and censoring. These effects are generally driven by the small dynamical range of the molecular gas observations, typically spanning about 1 order of magnitude, implying that CO measurements reach low detection limits ($\sim 1 \sigma$) at a level where measurements of SFR are still highly significant ($> 3 \sigma$). We will not be concerned with the intercept of the SK Law, which requires the knowledge of how each cloud, and with what efficiency, forms stars. Our models are purposely very simple, so that the effect of each parameter and its variations can be quantified.

While we will attempt to account for general trends in observational data as published in the recent literature, we will make only modest attempts to force an agreement between the data and our models by choosing ad-hoc parameters. We will, however, discuss the impact of each parameter on the observed trends and the direction of change that may produce an (or a better) agreement.

All logarithms in this paper are in base 10.

2. Model Description

We implement a very simple prescription for our model ‘galaxy’, in terms of its molecular cloud content, using some standard results for the mass function and other properties of the clouds (e.g., see summary in Blitz & Rosolowsky 2004). We term this model our Default Model, and it will be our starting point for investigating stochastic and geometrical effects.

In this section we provide the scaling relations and assumptions that we have used in our Monte Carlo simulations. For the molecular clouds, the scaling relations are mainly those of our own Milky Way, which we consider an adequate assumption for many of the late-type, star-forming spirals published in the literature. We will also assume that our model galaxy is observed face-on, since many published results have been de-projected for inclination.

The mass function of molecular clouds in the Milky Way and the less than a handful nearby galaxies that have been observed with sufficient resolution and mapping size can be described as:

$$dN/dM_{H_2} \propto M_{H_2}^\alpha, \quad (3)$$

with $\alpha \sim (-1.5) - (-2.9)$ (Solomon et al. 1987; Heyer, Carpenter & Snell 2001; Mizuno et al. 2001; Engargiola et al. 2003; Rosolowsky 2005, 2007; Blitz et al. 2007; Wong et al. 2011; Gratier et al. 2011). We choose a mean value $\alpha = -2$ as representative for our Default Model (see Gratier et al. 2011); we will, however, investigate later in this paper the effects of changing α , since the differences in α from galaxy to galaxy appear to be real, and not driven by measurement uncertainties (Rosolowsky 2005).

The mass of each cloud is related to its radius via the relation (Solomon et al. 1987):

$$M_{H_2}/(3 \times 10^4 M_\odot) = [R/(10 \text{ pc})]^2, \quad (4)$$

in the mass range $500 - 3 \times 10^7 M_\odot$. Equation 4 is equivalent to a constant cloud surface density, and is one of Larson’s Laws (Larson 1981). The clouds mean surface density of $\sim 100 M_\odot \text{ pc}^{-2}$ implied by equation 4 is in the range observed for Milky Way clouds (Heyer et al. 2009). Higher values for the cloud mean surface density (e.g., Solomon et al. 1987; Bolatto et al. 2008) would simply produce a rigid shift of the simulated data toward larger values of Σ_{H_2} . We do not attempt to model the variations in cloud surface density observed by Heyer et al. (2009), although these are likely to be real. The cloud mass range is chosen to encompass not only the observed range in our own Milky Way and other Local Group galaxies (that have masses typically not larger than $\sim 3 \times 10^6 M_\odot$, Wilson & Scoville

1990; Rosolowsky 2005; Engargiola et al. 2003; Blitz et al. 2007), but also to account for the potential presence of giant molecular associations with masses as large as 10^7 – 10^8 M_\odot in some star-forming galaxies (Koda et al. 2009). We will explore later the impact of lower high-mass cut-offs for the GMCs. The proportionality constant between the mass and radius of the GMC is derived from MW studies; changing it causes a change in the gas surface density of the Observed SK Law. For instance, decreasing the radius by 10% at constant cloud mass causes the final gas surface densities to be on average 20% higher. Our Default model includes a $\sigma_R \sim 60\%$ gaussian dispersion in the mass-radius relation, consistent with what has been observed in the MW and neighboring galaxies (Blitz & Rosolowsky 2004).

Since we do not model the gas density profile within each cloud, we cannot follow the customary approach of relating the density of the SFR to the density of the gas (e.g., Schmidt 1959; Wyse & Silk 1989; Kennicutt 1998). However, a power law relation between SFR and gas densities implies a power law relation between SFR and cloud mass. This is immediately seen for a linear correlation between ρ_{SFR} and ρ_{H_2} , i.e., $\rho_{SFR} \propto \rho_{H_2}$ implies $SFR \propto M_{H_2}$. For power-law correlations with slope >1 , we seek guidance from observational data. For the clouds listed in Heiderman et al. (2010), we derive $\rho_{SFR} \propto \rho_{H_2}^{1.7}$ and $SFR \propto M_{H_2}^{1.3}$ for simple assumptions of the clouds' geometry. Furthermore, a direct relationship between SFR and dense ($n(H_2) > 10^4$ cm^{-3}) gas mass appears to be implied by data on molecular clouds within 0.5 kpc of the Sun (Lada, Lombardi & Alves 2010). We thus relate each cloud to a star formation rate via the relation:

$$SFR/(M_\odot \text{ yr}^{-1}) \propto (M_{H_2}/M_\odot)^\beta, \quad (5)$$

where we will test cases with $\beta=1.0$, 1.5, and 2.0. The normalization for equation 5 is arbitrary in our model, and we use the results of Kennicutt et al. (2007), Bigiel et al. (2008) and Liu et al. (2011) to set a reasonable range for the observed SFR surface density. In particular, for $\beta=1$, we assume the star formation efficiency, $SFR/M_{H_2}=5.25 \times 10^{-10}$ yr^{-1} (Leroy et al. 2008; Bigiel et al. 2011).

The exponent β of equation 5 is not the same as γ_{H_2} in the SK Law, the latter being the result of area-averages in both gas and SFR surface densities. In order to ensure some variation in the SFR-gas mass relation above, we insert an artificial dispersion given by a gaussian distribution with $\sigma(\log SFR) = 0.3$ dex in equation 5, as a starting assumption. This means that any cloud with expected SFR as given by equation 5 will be attributed a value between roughly 1/2 SFR and 2 SFR (1 σ). The actual dispersion in the SFR-cloud mass relation is basically unknown at this stage, although Enoch et al. (2007) find about a factor 3 dispersion in the dense core fraction of three Milky Way molecular clouds, thus justifying our $\pm 2x$ choice. Lada, Lombardi & Alves (2010) reports the case of two nearby molecular clouds with similar gas masses and a factor 10 difference in SFR; this case corresponds to a

3 σ –5 σ event for our parameter choice. We will later explore the impact of our assumption.

The observed SFR will be assumed to be extinction-free, and we do not introduce effects of dust attenuation in our simulations. This is reasonable, especially as more recent studies have employed SFR indicators that combine optical/UV and infrared tracers, and should therefore provide a fully extinction-corrected view of star formation in galaxies (Kennicutt et al. 2007; Bigiel et al. 2008; Verley et al. 2010).

We simulate our ‘sub-galactic regions’ as square areas with sides in the range 200 pc–5 kpc, thus covering the majority of sizes probed in the literature (Kennicutt et al. 2007; Bigiel et al. 2008; Blanc et al. 2009; Verley et al. 2010; Onodera et al. 2010; Momose et al. 2010). Although we probe sizes as small as 200 pc, we should note that the radius of the largest cloud in our model is about 300 pc (and the smallest is a little over 1 pc in radius, equation 4). However, the largest measured CO cloud radii are smaller than 100 pc both in the Milky Way and M33 (Wilson & Scoville 1990; Engargiola et al. 2003; Rosolowsky et al. 2003).

The boundary for the smallest region size, 200 pc, in our simulations aims at avoiding stochastic sampling effects of the stellar Initial Mass Function (IMF). The total mean H₂ mass in a square area of 200 pc side obtained from our simulations is around $2.5 \times 10^6 M_{\odot}$, corresponding to a $\text{SFR} \sim 1.3 \times 10^{-3} M_{\odot} \text{ yr}^{-1}$ for the star formation efficiency given above. This SFR corresponds to the minimum value below which the stochastic sampling of the IMF significantly affects the ionizing photon rate of a stellar cluster, and, therefore, any SFR indicator based on the ionizing photon rate (e.g., extinction-corrected H α , Lee et al. 2009; Corbelli et al. 2009). Another way to look at this limit is to recall that the above SFR produces a $\sim 1.3 \times 10^4 M_{\odot}$ stellar cluster over a 10^7 yr timescale. This timescale is roughly the crossing time of our smallest region, for stellar velocities $\gtrsim 10 \text{ km s}^{-1}$, and is equivalent to or smaller than a typical cloud lifetime (\sim a few $\times 10^7$ yr, Hartmann, Ballesteros-Paredes & Bergin 2001; Scoville & Wilson 2004; Kawamura et al. 2009). For a $\approx 10^4 M_{\odot}$ mass in stars, the scatter on the ionizing photon rate due to stochastic IMF sampling is around 20% (Villaverde, Cerviño & Luridiana 2010), for a Kroupa IMF (Kroupa 2001). If the UV stellar continuum is used to trace the SFR, the limiting SFR below which stochastic sampling becomes an issue is about 3 times lower than for H α (Lee et al. 2011). In this case, however, there may be concerns about UV stellar continuum tracing star formation over timescales $\gtrsim 100$ Myr, which may be longer than the lifetimes of molecular clouds (Hartmann, Ballesteros-Paredes & Bergin 2001; Elmegreen 2007; Kawamura et al. 2009).

We simulate covering factors for each area drawn randomly in the range cf_{min} – cf_{max} , in order to approximate the range of molecular cloud covering factors in the disks of star-forming galaxies as a function of location (arm/inter-arm regions) and galactocentric dis-

tance (central and outer regions). This is in agreement with the interpretation by Leroy et al. (2009) that variations in molecular gas surface density over large areas are an indication of varying covering factors of the area by clouds, if the cloud surface densities are roughly constant (Solomon et al. 1987, see, however, Heyer et al. (2009)). In addition to a constant distribution of covering factors between cf_{min} and cf_{max} , we attempt to simulate the observed larger frequency of low covering factors (Leroy et al. 2009) via the exponential distribution:

$$N_{reg}(cf) = 74 \times e^{(-4.3 \times cf)}, \quad (6)$$

where N_{reg} is the number of regions with covering factor cf drawn within the range cf_{min} – cf_{max} . With equation 6, we simulate about 50 times more regions with $cf=0.1$ than regions with $cf=1.0$. Although the exact ratio between these two extremes is not characterized yet (and also depends on the region’s size), we adopt the uniform distribution of covering factors and the distribution given by equation 6 as a reasonable bracket for conditions in external galaxies, where areas of low surface density are more common than those of high surface density.

Electing to fill the area, rather than a volume (i.e., by filling the thickness of the molecular disk with clouds), is equivalent to assuming that molecular clouds form a single layer in a face-on galaxy. This is a reasonable assumption in light of results for the low-inclination Large Magellanic Cloud (Fukui & Kawamura 2010) and of the fact that the mean thickness of the MW molecular disk is only about 120 pc (Scoville & Sanders 1987). For completeness, however, we will also explore the case in which volumes with given area and thickness of 120 pc are populated with clouds, with filling factors randomly drawn within a given range ff_{min} – ff_{max} . For the volume filling, we assume that SFR tracers can penetrate the entire thickness of the molecular disk. From an operational point of view, the detection of recent star formation either inside a molecular cloud or through a series of clouds will likely require use of a far-infrared SFR indicator, thus requiring that the molecular clouds are globally (as opposed to locally) optically thin to far-infrared light. This may occur if the optically thick core of the clouds has a small filling factor.

The baseline parameters outlined above form our Default Model. Our Monte Carlo simulations generate a random cloud in the mass range specified in equation 4 and with the mass distribution of equation 3. The cloud is then assigned a radius and a SFR, as specified in equations 4 and 5, which then get randomly scattered according to Gaussian distributions with σ_R and σ_{SFR} , respectively. The area of the cloud is subtracted from a pre-specified area to which a random covering factor cf , either with a uniform distribution or with a distribution function described by equation 6, in the range cf_{min} – cf_{max} has been attributed. Clouds are generated until $cf \times \text{area}$ is fully covered. The surface density of H_2 mass and SFR is finally calculated by dividing the total H_2 cloud mass and total SFR in

each area bin by the area itself. In keeping with standard conventions, we express the SFR surface density Σ_{SFR} in units of $M_{\odot} \text{ yr}^{-1} \text{ kpc}^{-2}$ and the H_2 mass surface density Σ_{H2} in units of $M_{\odot} \text{ pc}^{-2}$ (Kennicutt 1989). Additionally, scatter is added to the gas surface densities, to simulate measurement errors; we set the scale such that $\Sigma_{H2} \sim 6.5 M_{\odot} \text{ pc}^{-2}$ is detected at the 3σ level, and realizations with lower Σ_{H2} are not included in the fits. The boundary at $\Sigma_{H2} \sim 6.5 M_{\odot} \text{ pc}^{-2}$ is selected to ensure a dynamical range along the Σ_{H2} axis comparable to that of most observational data, which is usually one order of magnitude or more. In the next section, we evaluate the impact of this choice against lower or higher detection limits, and smaller or larger dynamical ranges. We do not add an analogous scatter component to Σ_{SFR} , since the SFRs in galaxies are generally measured with significantly higher confidence levels than Σ_{H2} .

For each set of parameter choices, 10,000–20,000 realizations (areas) are generated, to avoid shot noise effects. The Observed SK Law, equation 2, is then derived by applying an ordinary least-square (OLS) bi-sector linear fitting (Isobe et al. 1990) to the pairs of Σ_{SFR} – Σ_{H2} realizations in log–log space, thus treating our simulations in a similar fashion as most actual data. We recall that this method produces the same results, within the uncertainties, when fitting X versus Y or Y versus X. In section 3.3, we evaluate the results of the OLS bi-sector linear fitting against another often-used fitting method: the bi-linear regression fit (e.g., routines like FITEXY in the Numerical Recipes, Press et al. 2007). The latter method, by including uncertainties in both axis, produces also similar results in the X–Y and Y–X planes. The results from the Default Model are reported in the section 3.1, followed by an analysis of the changes induced on both γ_{H2} and σ_{H2} by variations in the parameters of the Default Model.

3. Analysis

3.1. The Observed SK Law for the Default Model

The results of our Default Model simulations are shown in Figures 1– 3, where we have chosen $cf_{min}=0.10$ and $cf_{max}=1.0$. Figures 1 and the top panels of Figure 3 report the results for a uniform distribution in covering factors, while Figures 2 and the bottom panels of Figure 3 report the same results obtained for the covering factor distribution of equation 6. In Figures 1 and 2, the three panels show the simulated data and the best fit lines in the $\text{Log}(\Sigma_{H2})$ – $\text{Log}(\Sigma_{SFR})$ plot, for selected region sizes in the range 200–1,000 pc, and for the three $\beta=1.0$, 1.5, and 2.0. There is an obvious increase in both the slope and the dispersion perpendicular to the mean of the scaling relations, going from shallow ($\beta=1$) to steeper ($\beta=2$) SFR–gas cloud mass relations (equation 5). A more subtle effect

is observed within each panel, with both slope and dispersion about the mean decreasing from small to large region sizes. These trends are more evident in Figure 3, where the measured values of γ_{H2} and σ_{H2} are shown as a function of region’s size from 200 pc to 5 kpc. In all cases, a detection ‘limit’ at $\Sigma_{H2} = 6.5 \text{ M}_{\odot} \text{ pc}^{-2}$ ($\text{Log}(\Sigma_{H2})=0.8$) is applied prior to fitting the data with a straight line, again to simulate standard measurement approaches that typically remove data below a set detection limit. With this selection, our simulated data span a dynamical range of $\sim 1\text{--}1.5$ orders of magnitude in Σ_{H2} , similar to the ranges measured in star-forming galaxies (e.g. Kennicutt et al. 2007; Bigiel et al. 2008; Blanc et al. 2009; Onodera et al. 2010; Momose et al. 2010; Liu et al. 2011). As expected from the choice of a common low-end detection limit at all region sizes, the largest dynamical range, $\sim 30X$, is spanned at the smallest region size and the range decreases down to about one order of magnitude at the largest size (Figures 1 and 2). Larger dynamical ranges at fixed Σ_{H2} detection limit can be obtained by requiring the cloud mean surface density to be higher than our selected value of $100 \text{ M}_{\odot} \text{ pc}^{-2}$ (see, e.g., Solomon et al. 1987; Bolatto et al. 2008).

At constant β , we observe a variation in the *measured* slope γ_{H2} : it decreases as a function of increasing sampling region’s size (Figure 3). For instance, for $\beta=2$ and a uniform distribution of covering factors, the measured slope goes from $\gamma_{H2} \sim 2.6$ at 200 pc down to $\gamma_{H2} \sim 1.1$ in a 5 kpc size region (top-left panel of Figure 3). A similar trend is observed for a distribution of covering factors as given by equation 6 (bottom-left panel of Figure 3). Thus, the values of γ_{H2} do not reproduce β , for $\beta > 1$. The rate of change, however, decreases for decreasing β , and at $\beta=1$ the measured slope changes from $\gamma_{H2} \sim 1.05\text{--}1.1$ at 200 pc to $\gamma_{H2} \sim 1.0$ at 5 kpc, hence providing a closer estimate of the actual value of β at virtually all sizes.

The main effect of changing the distribution of cloud covering factors from uniform to exponentially-weighted towards low values is to increase the density of points at $\Sigma_{H2} \lesssim 20 \text{ M}_{\odot} \text{ pc}^{-2}$ (Figure 2). This provides a closer resemblance to observational relations (e.g. Liu et al. 2011): once the SFR dynamical range in data and simulations is matched, the *mean* SFR value in the simulations is also closer to what measured in actual galaxies (section 4.2). However, the effect on the measured slope γ_{H2} and scatter σ_{H2} is small, although it is in the direction of systematically increasing both quantities (Figure 3); for instance, the slope increases by 0.04–0.14, with the exact value depending on both β and the region’s size, but always corresponding to less than 6% variation.

A trend that will remain common to the Default Model and any modification that will be analyzed in the next sections is the tendency for the measured slope γ_{H2} to converge to a value of ~ 1 at large sampling sizes, independently of the value of β . This is due to the fact that at large region sizes the cloud function will be fully sampled even for small values

of the covering factor, thus decreasing the contrast from region to region, and flattening the Observed SK Law to a linear correlation.

Similarly to γ_{H2} , the dispersion of the data about the mean trend, σ_{H2} , is a function of both β and the sampling size (Figure 3, right panels). It increases for increasing β and decreases for increasing size. The increase with β reflects the larger impact that stochastic sampling has on the larger, more strongly star-forming, clouds at small regions sizes. The decrease with increasing sampling size mirrors the same considerations made for γ_{H2} above: as the region increases, the cloud mass function becomes fully sampled at all covering factors, and the scatter decreases considerably.

In order to quantify our statements about the stochastic sampling of the cloud mass function, Figure 4 shows the mean number of clouds and the mean cloud mass as a function of region size, for the exponentially decreasing cloud covering factors. A uniform distribution of covering factors gives similar results. These are independent of β , since they only concern the molecular clouds and the covering factor of each region. Use of mean values is appropriate, since the cloud mass and number distributions in each region are almost symmetric about a peak value, and the latter is close to the mean value (Figure 4, bottom panel). The top-left panel show that while the mean number of clouds clearly increases for increasing region size, the trend slightly (by 50% or less) exceeds the expectation of cloud numbers increasing as the square of the region size, except for the largest sizes probed, i.e., regions $\gtrsim 1\text{--}2$ kpc in size. Similarly, the mean cloud mass increases, also by a maximum of 50%, as a function of region size, and tends to level off only for regions $\gtrsim 1\text{--}2$ kpc in size. This shows that the cloud mass function we implement is fully sampled only for regions larger than $\sim 1\text{--}2$ kpc, and stochastic sampling is an important factor for smaller regions.

In the rest of the paper, we will preeminently report results based on the Default Model with an exponentially decreasing distribution of cloud covering factors (equation 6), for the following two reasons: (1) all other parameters being equal, the two distributions, uniform and exponential, produce generally small differences in γ_2 and σ_{H2} ; (2) equation 6 likely better approximates the conditions in external galaxies. In fact, for an exponential distribution of cloud covering factors, we derive a mean SFR from the simulations which is within 50% of the mean value measured in the nearby galaxy M51a (Kennicutt et al. 2007), after matching the SFR dynamical range values between model and observations (e.g., Figure 2). Conversely, a uniform distribution of cloud covering factors yields mean SFR values that are a factor $\gtrsim 2$ too high relative to what measured in data. This provides a justification for using equation 6 in what follows, although the uniform case will be discussed in parallel whenever relevant.

3.2. Scatter in the SFR–Cloud Mass Relation

We test the impact of our choice of $\sigma(\log SFR)=0.3$ (see section 2), by running our simulations again, but with two more extreme values for the gaussian standard deviation: $\sigma(\log SFR)=0$ (i.e., zero scatter, implying a deterministic relation between SFR and cloud mass) and $\sigma(\log SFR)=0.6$ (i.e., a factor 4 variation in SFR at fixed cloud mass). Figure 5 shows the changes in γ_{H2} and σ_{H2} as a function of both β and region size for these two choices of $\sigma(\log SFR)$. The general trend for γ_{H2} to decrease as a function of increasing region size, and converge towards values ≈ 1 , persists even for these other choices of the scatter between SFR and cloud mass. Most importantly, the trend persists even when there is no scatter in the relation between SFR and cloud mass. The measured slope also steepens for increasing $\sigma(\log SFR)$, at constant β and region size; for instance, in the case of $\beta=1$ and size=300 pc, the measured slope goes from $\gamma_{H2} \sim 1$ to 1.2 for $\sigma(\log SFR)$ that increases from 0 to 0.6. Increasing the scatter in the relation between SFR and cloud mass (equation 5), thus, causes the slope to become steeper, and this result persists at all ‘detection limits’ in Σ_{H2} and even in the absence of a limit. The steepening is the result of the interplay between $\sigma(\log SFR)$ and the uncertainties along the x-axis (Σ_{H2}).

The measured scatter σ_{H2} decreases for increasing region size, similarly to what is observed in Figure 3, even when varying the value of $\sigma(\log SFR)$. Interestingly, non-negligible values of σ_{H2} are measured also for $\sigma(\log SFR)=0$. This scatter purely reflects the fact that, for most of the regions we consider, the cloud mass function is stochastically sampled, rather than fully sampled, especially when accounting that each region is filled with clouds according to a randomly selected covering factor between 10% and 100%. This effect is exacerbated for increasing values of β , since higher weight (i.e., SFR) is given to the large clouds that are most subject to the effects of stochasticity.

The above experiment highlights an important degeneracy: γ_{H2} and σ_{H2} can increase both by increasing the slope β and by increasing the scatter in the SFR–cloud mass relation. However, σ_{H2} increases fractionally more than γ_{H2} when scatter increases (compare Figure 3, right panels, with Figure 5), which can provide a useful discriminant for observational data.

3.3. The Origin of the Scatter in the Observed SK Law

We have seen in the previous section that the Observed SK Law preserves a measurable scatter even in the absence of intrinsic scatter in the relation between SFR and cloud mass (equation 5). Here we investigate the source of the scatter in our simulations. To fix ideas, we will concentrate on the case with $\beta=1.5$ and region size 200 pc. As before, we consider

the case of an exponential distribution of cloud covering factors. For $\sigma(\log SFR)=0$, the Observed SK Law in this case has $\gamma_{H2}=1.76$ and $\sigma_{H2}=0.49$. Throughout this section, the SFR–mass relation (equation 5) is set to zero dispersion.

We begin our test by removing all sources of dispersion from the simulations, including those related to each region’s covering factor, to the mass–radius relation, and to the simulated scatter in the Σ_{H2} measurements. We fill each region to 100% of the area, i.e., $cf_{min}=cf_{max}=1$. We also remove any detection limit in the Σ_{H2} generated distribution. However, we are still randomly sampling the clouds within each region, according to the distribution of equation 3, with our default choice of $\alpha=-2$. With these assumptions, we generate an Observed SK Law with a negligible dynamical range in Σ_{H2} , of about 0.02 dex in logarithm scale, centered around $\log(\Sigma_{H2}) \sim 2$. This is a direct consequence of equation 4; since the relation between cloud mass and radius implies a constant cloud surface density, filling the entire area with clouds ($cf=1$) produces bins with the same Σ_{H2} values. Despite this, we already observe a dispersion of $\sigma_{H2}=0.33$ along the Σ_{SFR} axis, due to the combination of the non–linear relation between SF and M_{H2} and the random sampling of the cloud mass distribution within each region. The combination of the two effects is indeed crucial for the dispersion. The same simulation, but with $\beta=1$ instead of 1.5, produces a distribution of points that has the same negligible dynamical range, and $\sigma_{H2}=0$, i.e., zero scatter along the Σ_{SFR} axis.

We now proceed by adding one ingredient: random covering factor between cf_{min} and cf_{max} . We keep $cf_{max}=1$ and vary cf_{min} between 0.05 and 0.4. In this case, the main effect is an increase in the dynamical range of the simulated data: at $cf_{min}=0.05$, $\log(\Sigma_{H2})$ spans the range ~ 0.7 –2, decreasing to 1–2 for $cf_{min}=0.1$, and progressively decreasing down to 1.6–2 for $cf_{min}=0.4$. For $cf_{min}=0.05$ to 0.15 the OLS bi–sector fit gives a slope $\gamma_{H2} \sim 1.75 \sim \beta$ within the 1σ measurement error. For $cf_{min} > 0.15$ the fitted slope becomes steeper, owing to the decreasing dynamical range spanned by the data. However, the dispersion about the best fitting line remain virtually unaffected, with $\sigma_{H2}=0.35$. The direct connection between dynamical range in Σ_{H2} and covering factor is again a direct consequence of equation 4 and the constant cloud surface density it implies.

The dispersion remains similarly unaltered when we fix $cf_{min}=0.10$ and vary cf_{max} in the range 0.60–1. Variations in the maximum value of the covering factor impact the high–end values of Σ_{H2} , which decrease from $\log(\Sigma_{H2}) \sim 2$ for $cf_{max}=1$ down to $\log(\Sigma_{H2}) \sim 1.8$ for $cf_{max}=0.60$. Thus, the main impact of the covering factor variation is on the dynamical range spanned by the ‘observed’ Σ_{H2} .

Keeping cf_{min} and cf_{max} at the Default Model values of 0.1 and 1, respectively, and adding scatter in the cloud mass–radius relation ($1\sigma=60\%$, similar to what is observed

in actual MW molecular clouds, Blitz & Rosolowsky 2004) further increases the dynamical range covered by the simulated data, from one order of magnitude to a factor $\gtrsim 60$ in Σ_{H_2} (Figure 6). Both slope and dispersion remain basically unchanged, at $\gamma_{H_2} \sim 1.73$ and $\sigma_{H_2} \sim 0.35$.

Re-adding into the simulations the measurement uncertainties for Σ_{H_2} , so that values at $\Sigma_{H_2} \sim 6.5 \text{ M}_\odot \text{ pc}^{-2}$ are detected at the 3σ level, changes the Σ_{SFR} – Σ_{H_2} distribution in more than one way. The dynamical range increases further relative to the previous cases, but almost exclusively in the direction of small Σ_{H_2} values (Figure 6), down to $\Sigma_{H_2} = 0.4 \text{ M}_\odot \text{ pc}^{-2}$. This reflects the fact that lower Σ_{H_2} values are detected at increasingly lower confidence. Furthermore, the distribution becomes markedly non-symmetric relative to the best fit line, reflecting the non-symmetric nature of scatter in a logarithmic plot. Finally, γ_{H_2} decreases significantly, down to $\gamma_{H_2} = 1.46$ and σ_{H_2} increases to its final value of 0.49. When we add a detection limit to Σ_{H_2} , γ_{H_2} increases back to the value 1.76 (Figure 5, top-left), while σ_{H_2} remains unchanged (Figure 5, top-right).

In summary, in the absence of scatter between SFR and cloud mass, there is still considerable scatter in the data about the best fitting line in the Σ_{SFR} – Σ_{H_2} plane, with $\sigma_{H_2} \sim 0.5$ at 200 pc for $\beta = 1.5$. About 60% of this scatter is due to the combination of the non-linear relation between SFR and M_{H_2} and stochastic sampling of the cloud mass function. This effect produces a little over 80% of the scatter σ_{H_2} for the $\beta = 2.0$ case (Figure 5, top-right). The remaining $\sim 40\%$ of the scatter for the $\beta = 1.5$ case is due to our modeled measurement uncertainties; the behavior of this second portion of the scatter reflects the non-symmetric nature of errors in logarithmic scale. For $\beta = 1$ only the latter portion of the scatter is present, implying that the values $\sigma_{H_2} \lesssim 0.2$ for $\beta = 1$ in Figure 5 (top-right) are due mainly to the effects of measurement uncertainties along the Σ_{H_2} axis.

3.3.1. Volume Filling versus Area Covering

The relative thinness of molecular disks implies that usually no more than 1–2 clouds overlap along a given line of sight for a face-on disk (Scoville & Sanders 1987; Kawamura et al. 2009). Furthermore, CO observations can often separate multiple clouds along a line of sight via the different velocity imprints of separate clouds. Although this helps justify the use of a bi-dimensional model for our simulated ‘galaxy’, it is worth investigating the general trend obtained in the case of a three-dimensional model where the dimension perpendicular to the area covered with clouds is 120 pc thick. This is on account that even if clouds overlapping along a line of sight can often be separated, their associated SFR usually cannot, as SFR tracers do not carry the same spectral information as CO data.

For this model, we choose a volume filling factor with $\text{ff}_{\min}=0.1$ and $\text{ff}_{\max}=1$; we limit our simulations to the simplest case in which no scatter is added to any relation or data, although we still retain an exponential distribution of cloud covering factors. For $\beta=1.5$ and 200 pc region size, we obtain $\gamma_{H2}=1.13$ with $\sigma_{H2}=0.22$. This should be compared with the analogous two-dimensional case above which gives $\gamma_{H2}=1.75$ with $\sigma_{H2}=0.35$. Filling a volume produces a significantly flatter slope and smaller dispersion about the mean trend in the $\Sigma_{SFR}-\Sigma_{H2}$ distribution than covering an area. The flattening of γ_{H2} cannot be simply attributed to variations in the dynamical range covered by the simulated data in the two cases, since they have similar ranges (1.1 dex versus 1 dex). However, our simulations do not include control on the shape of the volume to be filled, which affects the final result by allowing multiple clouds to be located along the line of sight. Indeed, a direct comparison of the volume-filling simulation with the area-covering simulation shows that the former fills each volume with about 6 times more clouds, that are about 20% less massive, on average than what the latter does. The combination of these effects produces a more effective averaging of the cloud mass distribution in the volume-filling case than in the area-covering case, thus yielding an overall flatter γ_{H2} slope.

Actual observations are likely to be in-between our two cases of areal-cover and volume-filling. In the next sections we limit our analysis to the two-dimensional case, although the result from this section should be kept in mind for any general conclusion.

3.4. Fitting Method, Range, and Data Censoring

In the previous sections, we have presented the baseline results for our Default Model, using the OLS bi-sector linear fitting. This is the same fitting approach adopted by a number of observational analyses of the SK Law (e.g. Blanc et al. 2009; Verley et al. 2010; Liu et al. 2011; Rahman et al. 2011). The advantage of the OLS bi-sector fitting is the ability to divide the locus of the data into two roughly equal-number areas; however, its disadvantage is that error bars on the data are not included in the fitting, and statistically insignificant data points get the same weight as significant ones (see discussion in Verley et al. 2010). Another routine often used to determine the slope and intercept of the Observed SK Law is the bi-linear regression fit (Kennicutt et al. 2007; Verley et al. 2010).

We compare the best fit slopes obtained with both the OSL bi-sector fit and the bi-linear regression fit in Figure 7, for both cases of the Default Model (left panel) and the model in which the relation between SFR and cloud mass has zero scatter in equation 5 ($\sigma(\log SFR)=0$, right panel). For both fitting methods, the best fit slope is a decreasing function of increasing region size, and in neither case the actual value of β is systematically

recovered (except for $\beta=1.0$ using the OLS fitting method). However, the bi-linear fit yields larger numerical values for γ_{H2} than the OLS fit, and the magnitude of the discrepancy is an increasing function of increasing β , decreasing region size, and increasing intrinsic scatter between the SFR and the cloud mass. For $\beta=1, 1.5$, and 2 , $\delta\gamma_{H2}/\gamma_{H2}(OLS) \sim 20\%-2\%$, $50\%-20\%$, and $80\%-30\%$, respectively, for regions in the range $200-2,000$ pc. The bi-linear fit method yields larger uncertainties, by a factor $3-15$, in the final uncertainty of γ_{H2} than the OLS fit, which is a better reflection of the scatter in our simulated data points.

Next we test the impact of measurement uncertainties. For most studies, the dominant source of uncertainty is the gas (CO or other molecular gas tracers) measurement, as tracers of SFR are usually detected at high significance even when 1σ detection limits are reached in CO. We can approach the problem of measurement uncertainties in two different ways: (1) by changing the significance level of our detection ‘limit’ in Σ_{H2} ; and (2) by varying the value of the detection limit. The former tests changes in γ_{H2} induced by the varying significance of the data, but preserving the full dynamical range of the simulated data points. The latter mimics variations in the dynamical range of observational data due to varying detection limits, and should test the impact of common data censoring procedures. In order to highlight trends, we concentrate our analysis on three representative region sizes: 200 pc, 500 pc, and 1 kpc. We use, from now on, the OLS bi-sector fitting as our default.

When varying the significance of the detection limit without changing the numerical value of the limit (set to $\Sigma_{H2} \sim 6.5 M_{\odot} \text{ pc}^{-2}$ in the Default Model), we measure an increase in γ_{H2} for increasing detection threshold between 1σ and 5σ , with most of the change concentrated between 1σ and 3σ (Figure 8). The change is generally modest, $\delta\gamma_{H2}/\gamma_{H2} \lesssim 15\%$ for $\beta=2$ and $\delta\gamma_{H2}/\gamma_{H2} \lesssim 5\%$ for $\beta=1$, at all sizes. The values of γ_{H2} become roughly constant for thresholds $\geq 3\sigma$, in our model, although they level off at different values for different region sizes, and recover β systematically only for the largest size (1 kpc).

Variations of the detection limit that vary the numerical value of the lowest valid data change the dynamical range of the data. Higher limits than our selected 3σ at $\Sigma_{H2} \sim 6.5 M_{\odot} \text{ pc}^{-2}$ will decrease the data range; vice versa for lower limits. For instance, going from a 3σ threshold to a 5σ one reduces the dynamical range by 0.45 dex in $\log(\Sigma_{H2})$ in our simulations. This attempts to mimic observational situations in which different detection thresholds may be chosen for the same data, and also addresses the issue of data censoring, especially for Σ_{H2} , which tends to have lower data significance than Σ_{SFR} for most observational cases. Figure 9 shows that varying the dynamical range of the data, together with their significance exacerbates variations in the observed slope, with larger changes in γ_{H2} between 1σ and 5σ than in the previous case (cf. Figure 8 with Figure 9). As before, the largest variations are observed for the largest values of β , with $\delta\gamma_{H2}/\gamma_{H2} \lesssim 50\%$ for $\beta=2$

and $\delta\gamma_{H2}/\gamma_{H2} \lesssim 35\%$ for $\beta=1$.

3.5. Variations in the H₂ Clouds Mass Function

The maximum mass of a molecular cloud in a galaxy is not necessarily a constant, although variations from galaxy to galaxy do not appear to be large. In the MW, M31, and LMC the maximum measured H₂ masses are about $1\text{--}3\times 10^6 M_\odot$ (Wilson & Scoville 1990; Rosolowsky 2005; Engargiola et al. 2003; Blitz et al. 2007), but the largest clouds could be smaller in the LMC, depending on identification techniques (Wong et al. 2011). Giant Molecular Associations, as massive as $10^7\text{--}10^8 M_\odot$, could be present in some galaxies (Koda et al. 2009). Conversely, the slope α of the cloud mass function (equation 3) varies considerably from galaxy to galaxy, with values that range from ~ -1.5 in the inner parts of the MW to $\sim -2.6/-2.9$ in M33 and the LMC (Engargiola et al. 2003; Rosolowsky 2005; Wong et al. 2011). The actual range of α might be smaller than the one just quoted, though; shallow values of α may be the result of cloud blending, while steep values may be due to fitting the mass function beyond the clouds high-end cut-off (Rosolowsky 2005). Nevertheless, the existence of a range of values for α is considered both physical and significant. Our Default Model uses $\alpha = -2.0$ and a maximum H₂ cloud mass of $3\times 10^7 M_\odot$, the latter to accommodate the Giant Molecular Associations identified by Koda et al. (2009) in the M51a galaxy. The normalization is set to allow one cloud to be formed with the maximum cloud mass $M_{cloud}(\text{max})$.

The impact of variations of $M_{cloud}(\text{max})$ and α is summarized in Figures 10 and 11. $M_{cloud}(\text{max})$ is changed from $3\times 10^5 M_\odot$ to $3\times 10^7 M_\odot$ (our Default Model value) in factor 10 increments of mass. Values of α considered are -1.5 , -2.0 (Default Model value), and -2.3 , which spans a range close to the observed one. Figure 10 shows the measured slope γ_{H2} and the dispersion σ_{H2} about the best fit line of the Observed SK Law in both cases. Variations in $M_{cloud}(\text{max})$ have a larger impact, in terms of fractional changes in γ_{H2} , than variations in α when $\beta > 1$, at least in the range explored here. As the maximum cloud mass decreases, γ_{H2} tends to values of unity and σ_{H2} decreases monotonically; for any value of the SFR–cloud mass power law index, $\gamma_{H2} \leq 1.2$ for $M_{cloud}(\text{max})=3\times 10^5 M_\odot$ and region sizes $\gtrsim 500$ pc. This behavior is in agreement with the expectation that for decreasing values of $M_{cloud}(\text{max})$, the cloud mass function is fully sampled for smaller region sizes and, for $\beta > 1$, less efficient star-forming clouds are included in the SFR accounting. Figure 11 supports this conclusion: for decreasing $M_{cloud}(\text{max})$, the mean number of clouds in a region increases, albeit modestly, while the mean cloud mass decreases.

An intuitive result can be obtained by setting all clouds to have the same mass, such

that at least one cloud is sampled by the smallest region simulated, i.e., $M_{cloud} < 3 \times 10^5 M_{\odot}$. In this case, $\gamma_{H2} = 1 \pm 0.1$, irrespective of region size, cloud size, or β . Also σ_{H2} has values that are typically a factor 3 or more smaller than the equivalent values obtained with a distribution of cloud sizes. If we set the clouds to have identical mass $M_{cloud} > 3 \times 10^5 M_{\odot}$, implying that the clouds are larger than the smallest simulated area, we obtain $\gamma_{H2} > 1$, but $\gamma_{H2} < \beta$ (for $\beta > 1$) with little variation as a function of region size. This is because, for identical clouds, all regions sample the same SFR surface density values, which then simply scales as the H_2 surface density. This result may help explain the trend of γ_{H2} in the bottom panels of Figure 10, which show a generally decreasing function for increasing α . A flatter cloud mass distribution ($\alpha = -1.5$) than that of our Default Model gives more uniform weight to all masses, which then flattens the trend in γ_{H2} .

Changes in the normalization of the cloud mass function have a small impact on the values of γ_{H2} . If we allow the normalization of the cloud mass function to be such that 100 clouds with value $M_{cloud}(\text{max})$ are produced, rather than 1 cloud, all values of γ_{H2} steepen by 0.03–0.04, for $M_{cloud}(\text{max}) = 3 \times 10^7 M_{\odot}$ and $\alpha = 2.0$. The steepening is still within 1–3 σ of the measured uncertainty in the slope, thus a small variation.

In summary, variations in the cloud mass function have a large impact on the resulting parameters of the Observed SK Law, for both changes in $M_{cloud}(\text{max})$ and α . Changes in the normalization of the cloud mass distribution produce small-to-negligible effects at all region sizes and β values explored in this paper.

4. Effects of Selection Biases in Star Formation

Our Default Model attributes star formation to each cloud that is sampled into a region according to equation 5, independently of the characteristics of the cloud. This is a simplistic approach that we will try to refine in this section.

As clouds become smaller and less massive their ability to condense into high density cores may decrease, and so will be their capability to form stars. This can be translated into a minimum cloud mass threshold for star formation in our simulations. Additionally, low-mass clouds will be less likely to form massive stars than larger mass clouds, thus will not contribute to SFR measurements that rely on massive star tracers (UV, $H\alpha$, ...). We can estimate the fraction of SFR lost to this effect, by assuming that clouds less massive than $\sim 3,000 M_{\odot}$ are unlikely to form UV-bright or ionizing stars. This implies that 16% of the SFR is not detected for $\beta = 1.0$, but the fraction decreases to less than 1% for $\beta = 1.5$ or higher. This reasoning, however, only applies if there is a direct correlation between cloud

mass and the most massive star formed (e.g. Weidner & Kroupa 2006). If star formation is a purely stochastic process (e.g. Calzetti et al. 2010), the stellar IMF will be fully sampled for large numbers of clouds, even if these are low-mass ones.

There are other reasons for implementing thresholds for star formation to cloud masses, and quantifying their effects on the Observed SK Law. One of the procedures employed in some recent papers, including Liu et al. (2011), prescribes the removal of an extended/diffuse component from the data that are used to measure the SFRs. This extended component can represent up to 50% of the total stellar emission (either as direct or as dust-reprocessed stellar light). Much debate is currently underway about whether the extended component is effectively unrelated to current star formation (i.e., the emission is tracing light from intermediate/old stellar populations), or whether it represents some low-level, unresolved star formation. In the former case, its removal prior to SFR measurements is justified, but it would not in the latter case.

If the diffuse component is unrelated to current star formation, studies that do not remove that component (e.g. Bigiel et al. 2008) add an artificial contribution to the SFR measurements. The addition of this background will affect measurements of both γ_{H2} and σ_{H2} , and we will quantify its impact in section 4.2.

4.1. Cloud Mass Threshold for Star Formation

Using the Default Model as a starting point, we model the SFR thresholds by removing a fraction of the SFR from the simulations. We specifically assign $SFR=0$ to H_2 clouds that are below a given mass threshold, $M_{cloud}(thr)$. Clouds below this threshold are still accounted for in the final census for the gas surface density, but they do not contribute to the SFR surface density.

As we can intuitively infer that selective removal of star formation from the small clouds will steepen the Observed SK Law, we quantify this effect for the flattest $SFR-M_{H2}$ relation we analyze, i.e., $\beta=1.0$. We consider the case in which 1/3, 1/2, and 60% of the total SFR is removed, on average, from each region, which corresponds to threshold cloud masses $M_{cloud}(thr)=10^{4.3} M_{\odot}$, $10^{5.1} M_{\odot}$, and $10^{5.6} M_{\odot}$, respectively (Figure 12).

As expected, a steepening of the Observed SK Law is observed, which is already significant when 33% of the SFR is removed, especially for region sizes smaller than ~ 1 kpc. Similar trends are observed for the scatter of the data about the mean trend, σ_{H2} .

The derivative of γ_{H2} becomes increasingly more negative as the SFR removal increases

up to $\sim 50\%$ (Figure 12, left), and then it flattens again for small region sizes. The derivative changes sign below 400 pc for the case with 60% of the star formation removed. For this case, a large fraction of bins do not contain any detectable star formation at small region sizes; this fraction is about 50% at 300 pc and 70% at 200 pc. This is due to the combined effects of region size and distribution of cloud covering factors, that tend to give preference to small (non star forming) clouds. Regions with small covering factors *and* a non-zero SFR, thus, crowd in the upper envelope of the $\Sigma_{SFR}-\Sigma_{H2}$ distribution, which results in smaller γ_{H2} values (flatter trends in the $\Sigma_{SFR}-\Sigma_{H2}$ plane). Larger size regions suffer progressively less from this selection problem, as do lower thresholds. The trend for the derivative of σ_{H2} is similar to that of γ_{H2} , except that a flattening of the trend with region size occurs when $\geq 60\%$ of the SFR is removed.

For a uniform distribution of cloud covering factors, the overall behavior is similar, but the effect is less pronounced: the derivative of γ_{H2} starts flattening again below 400 pc at 60% star formation removal (50% of the 200 pc bins contain star formation in this case). In general, a uniform distribution of covering factors gives values of γ_{H2} on average 0.05–0.1 smaller than reported in Figure 12, left panel, and values of σ_{H2} on average 0.02–0.05 smaller.

The changes in the derivative of the γ_{H2} and the σ_{H2} trends with region size for increasing values of the threshold are present for $\beta > 1$ as well. It should be noted that a given cloud mass threshold corresponds to a smaller fraction of the SFR removed in the case of $\beta > 1$; for instance, $M_{cloud}(thr)=10^{5.1} M_{\odot}$ removes only about 6% of the total SFR for $\beta=1.5$, as opposed to 50% for $\beta=1$.

4.2. Background Addition to Star Formation

We simulate the presence of a diffuse, uniform background in SFR data by adding a constant value to the SFR in each region of the Default Model, corresponding to a set fraction of the mean SFR value from all regions. Since the addition of a constant value will result in a general flattening of the Observed SK Law, we quantify this effect for the $\beta=1.5$ case.

The results are summarized in Figure 13. A constant background addition larger than 10% produces values of $\gamma_{H2} < \beta$, for any region size. For backgrounds equal or larger than 50%, the recovered $\gamma_{H2} \leq 1.05$ for all region sizes, and the slopes are flatter even than those for the case of $\beta=1.0$ with no background added (Figure 3, bottom panels). Analogous considerations apply to σ_{H2} . In the case of a uniform distribution of cloud covering factors, the qualitative trends are similar to those in Figure 13, with quantitative offsets in both γ_{H2} and σ_{H2} similar to those discussed in section 4.1.

The background levels used in Figure 13 are calculated as fractions of the mean SFR measured in the 10,000 realizations of each region size. As the mean SFR values reflect the distribution of covering factors, the background fractions correspond to higher absolute SFR values for the uniform distribution of cloud covering factors than for the exponentially decreasing one. One general consequence is that, at constant background fractions, the values of γ_{H2} generated with the former distribution are generally a little smaller, by $\Delta\gamma_{H2} \leq 0.05$, than those generated with the latter one.

5. The Azimuthally–Averaged SK Law

Many analyses derive the SK Law using azimuthally–averaged radial profiles of galaxies (e.g., Wong & Blitz 2002; Boissier et al. 2003; Heyer et al. 2004; Verley et al. 2010), rather than regions within galaxies. The advantage of radial profiles is the higher signal–to–noise ratio than can be obtained on individual measures. The main disadvantage is that the cloud mass function is averaged in regions that increase progressively in area with radius.

We modify the Default Model to simulate an azimuthally–averaged SK Law. We require that regions be annuli that grow in radius between R_{min} and R_{max} , in steps of R_{step} . For each annulus, we generate 200 independent realizations, to ensure sufficient statistical averaging. We also require that the lowest gas surface density value generated by our model is detected at the 5σ level, to mimic the higher signal–to–noise ratio typical of such analyses. This translates into requiring that $\Sigma_{H2}=3\text{ M}_{\odot}\text{ pc}^{-2}$ is detected at the 5σ level in our simulations. No other parameter of the Default Model is changed, in order to facilitate comparison with the individual region simulations.

The presence, within a single simulation, of regions of different total area helps increasing the dynamical range spanned by Σ_{H2} : it covers from $\Sigma_{H2}=3\text{ M}_{\odot}\text{ pc}^{-2}$ at the low–end to $\Sigma_{H2}=100\text{ M}_{\odot}\text{ pc}^{-2}$ at the high end, almost irrespectively of β and R_{max} . The dynamical range of Σ_{H2} for the azimuthally–averaged simulation is thus 2–3 times larger than in the case of individual regions, especially when compared with large region sizes. For simplicity, our simulations assume $R_{min}=R_{step}=200\text{ pc}$ (e.g., Heyer et al. 2004; Verley et al. 2010) and a variable R_{max} between 4 kpc and 14 kpc.

The best fit slopes γ_{H2} for the Observed SK Law and the parameter choices above are shown in Figure 14 for the three cases of $\beta=1.0$, 1.5, and 2.0, and a range of R_{max} values. Results for both the uniform and exponential distributions of cloud covering factors are shown. As may be expected from the results obtained in the previous sections, the azimuthally–averaged γ_{H2} is always lower than β for $\beta > 1.0$, and decreases for increasing

R_{max} . This result may be better understood with a specific example: for $R_{min}=200$ pc and $R_{max}=4$ kpc, the smallest area simulated is 0.13 kpc^2 and the largest is about 5 kpc^2 (corresponding to the largest annulus). The convolution of the contribution from all the annuli in a given simulation has the general effect of flattening the γ_{H2} slope relative to β . The case $\beta=1.0$ is an exception, with $\gamma_{H2} \approx 1$ at all R_{max} (Figure 14).

Our simulations do not include a dependence of the cloud covering factor on galactocentric distance, which has been suggested by Leroy et al. (2009). However, the comparison, at fixed β , between the slopes γ_{H2} of the uniform and exponential distributions of cloud covering factors in Figure 14 suggests that changes in the overall distribution of covering factors has a small impact on the measured slope: $\delta\gamma_{H2}/\gamma_{H2} \lesssim 8\%$ at $\beta=1.5$ for the two distributions we consider.

6. Discussion

6.1. Summary of Simulation Results

Despite the inevitable simplifications our models contain, a number of general trends can be garnered from the above analysis. There is a strong dependence of the slope γ_{H2} of the Observed SK Law on the physical size of the region sampled; specifically, at fixed exponent β of the intrinsic relation between SFR and cloud mass ($\text{SFR} \propto M_{H2}^\beta$, equation 5), γ_{H2} decreases for increasing region's size. The derivative of the trend is larger, in absolute value, for higher β (e.g., Figures 3 and 5). In fact, for $\beta=1$, γ_{H2} rarely deviates from a value of ≈ 1 , except when the scatter between SFR and M_{H2} is a factor ~ 4 or larger (Figure 5, bottom panels). For $\beta > 1$, γ_{H2} usually transitions from $\gamma_{H2} > \beta$ at small scales ($\lesssim 500$ pc) to $\gamma_{H2} < \beta$ at large scales ($\gtrsim 1,000$ pc), again with the exception of scenarios in which the scatter between SFR and M_{H2} is large. This transition scale is strongly dependent on the maximum cloud mass, $M_{cloud}(\text{max})$, that can form in the galaxy, and less strongly dependent on the power law exponent α of the cloud mass function (Figure 10). For $M_{cloud}(\text{max}) \lesssim 10^{6.5} M_\odot$, i.e., a factor 10 or more lower than our default assumption, $\gamma_{H2} < \beta$ at ~ 500 pc and larger sizes.

The values of γ_{H2} are influenced by the fitting procedure and by the dynamical range of the data, as already remarked by other authors on the basis of observational results (e.g. Blanc et al. 2009; Verley et al. 2010; Liu et al. 2011). If instead of using the OLS bi-sector fitting, we employ the FITEXY routine, i.e., a χ^2 -minimization procedure that weights the result by the uncertainty along both the X and Y axis, the resulting values of γ_{H2} are systematically higher than those produced by the OLS bi-sector method (Figure 7; see, also Verley et al. 2010), and the discrepancy increases for decreasing region sizes. For $\beta=1, 1.5$,

and 2, $\delta\gamma_{H2}/\gamma_{H2}(OLS) \sim 20\%-2\%$, $50\%-20\%$, and $80\%-30\%$, respectively, for regions in the range 200–2,000 pc. The general trend is for the OLS and FITEXY slopes to converge for both increasing region sizes and for decreasing values of β , since in both cases γ_{H2} tends to values of unity. The formal uncertainty on $\gamma_{H2}(FITEXY)$ is, however, much larger than that produced by the OLS bi-sector fitting routine, by factors 3–15 for the three β values considered.

The dynamical range along the molecular gas surface density axis has a major influence on the value of γ_{H2} , in the sense that smaller dynamical ranges (e.g., stronger censoring or higher thresholds for the significance of the observational data) produce steeper values of γ_{H2} (Figure 9). The relation between the values of γ_{H2} and β is a complex function of both the dynamical range and the region size considered. However, a common result is for uncensored data to yield $\gamma_{H2} < \beta$ on of both the dynamical range and the region size considered. However, a common result is for uncensored data to yield $\gamma_{H2} < \beta$ at virtually any region size and any β . This is partly due to the non-symmetric nature of data scatter when projected along logarithmic axes.

Another notable influence to the values of γ_{H2} is given by the scatter in the SFR–cloud mass relation (Figure 5). The larger the scatter, the larger the value of γ_{H2} : for instance, for $\beta=1$, $\gamma_{H2}=1$ for zero scatter between SFR and cloud mass and $\gamma_{H2} \sim 1.2$ for a factor 4 scatter (1σ), at region sizes $\lesssim 700$ pc, and an exponential distribution of cloud covering factors. The fractional difference is higher for $\beta=1$ ($\sim 25\%$) than for higher values of β ($\lesssim 10\%-15\%$). The same result holds for σ_{H2} , which increases both for increasing β and increasing scatter in the SFR–cloud mass relation. This produces a potential degeneracy between high- β and high-scatter, although σ_{H2} increases faster for large scatter than γ_{H2} .

The slope γ_{H2} converges towards values of 1 at large region sizes, for all values of β analyzed in this paper ($\beta=1, 1.5, 2$). This is a reflection of the fact that, as the region’s size increases, the cloud mass function becomes better sampled. Thus, any difference between regions in the same realization (‘galaxy’) will mostly be due to differences in the covering factor, and the ‘data’ will start lining up along a line with slope=1 in the $\text{Log}(\Sigma_{SFR})$ – $\text{Log}(\Sigma_{H2})$ plane. The convergence occurs at region sizes $\gtrsim 2$ kpc if $M_{cloud}(\text{max})=10^{7.5} M_{\odot}$, but quickly decreases down to 1 kpc for $M_{cloud}(\text{max}) < 10^{6.5} M_{\odot}$ (Figure 10). Our simulation results agree well with the observational results of Schruba et al. (2010), where they find that regions centered on CO peaks produce similar gas depletion timescales as regions centered on H α peaks in M33 once such regions have diameters of about or larger than 1 kpc. The Schruba et al. (2010) result implies that 1 kpc is about the scale where both the HII region luminosity function and the cloud mass function are fully sampled; the latter is reproduced by our simulations once we take into account that $M_{cloud}(\text{max}) \sim 10^6 M_{\odot}$ in M33 (Engargiola et al.

2003).

The scatter of the ‘data’ about the best fitting line, σ_{H2} , is always significant even when there is no scatter in the SFR–cloud mass relation (Figure 5, top–right), and is due to a combination of effects: (1) measurement uncertainties along the Σ_{H2} axis, which affects ‘data’ for any value of β ; (2) the combination of a non–linear SFR– M_{H2} relation with random sampling of the cloud mass function, which affects only cases with $\beta > 1$. The first contribution produces a minimum plateau of $\sigma_{H2} \sim 0.1$ – 0.2 at $\beta=1$, while the second contribution increases σ_{H2} with increasing β . Expectedly, all values of σ_{H2} increase at fixed region size and β if the scatter in the SFR– M_{H2} relation increases. Like γ_{H2} , σ_{H2} decreases for increasing region’s size, implying that, as the cloud mass function becomes better sampled at larger sizes, so does the SFR.

Additions of SFR thresholds, as a consequence of either physical mechanisms (e.g., the lowest mass clouds cannot form massive enough stars to ionize the gas or emit in the UV) or selection biases, has the general effect of steepening γ_{H2} and increasing σ_{H2} (Figure 12). Conversely, the addition of a uniform contribution to the SFR axis (e.g., a background emission which, although unrelated to the current star formation, is included in the census of SFR) has the general effect of flattening γ_{H2} and reducing σ_{H2} .

Finally, analyses of azimuthally–averaged data should generally recover $\gamma_{H2} < \beta$ for $\beta > 1$ and $\gamma_{H2} \sim \beta$ for $\beta=1$ (Figure 14). The ‘flattening’ of γ_{H2} is an effect of averaging regions with a range of sizes when annuli of increasing radius are considered in such analyses.

6.2. Comparison with Observations

Given all the factors that can influence the observed slope of the SK Law and the scatter about the best fit line, it is perhaps not surprising that analyses in the literature have yielded many different, and sometimes contrasting, results. In this section, we compare our simulations against a subset of observational results, explicitly those results for which we are familiar with or can reconstruct the assumptions and choices built into the analysis (e.g., detection limits for the data, treatment of the background in the SFR data, fitting routines, etc.). A caveat is that our pixel–based simulations can only be compared with observations treated in a similar fashion, and are not immediately adaptable to measurements that use specific selection criteria for the galactic regions (e.g., regions selected to be peaks of SFR).

6.2.1. Individual Galaxies: M51a and NGC3521

We begin by comparing our simulations to the observational results obtained by our group. Liu et al. (2011) derived the Observed SK Law in the nearby galaxies M51a and NGC3521, for a variety of region sizes and detection limits. The authors derive the SFR maps for those two galaxies from a combination of both $H\alpha$ and $24\ \mu\text{m}$ emission and far-UV (FUV) and $24\ \mu\text{m}$ emission, following the calibrations of Calzetti et al. (2007) and Bigiel et al. (2008), which account for both the obscured and unobscured portions of the SFR. Liu et al. (2011) also remove a low-frequency emission from the $H\alpha$, FUV, and $24\ \mu\text{m}$ images of both galaxies, at the level of about 50% of the total emission in each band. Their stated reason for this removal is that the diffuse, low-frequency emission is likely not directly associated with the SFR traced by the molecular gas in a given region. We report the data from Liu et al. (2011) in Figure 15, with the region sizes given by the square root of the de-projected area of each galaxy bin. For each of the two galaxies, we adopt two extreme values of the inclination (20° – 42° for M51a and 65° – 73° for NGC3521), to account for uncertainties in this parameter as well. For each value of β , we show in Figure 15 a modification of the Default Model that most closely accounts for the observed trend in both γ_{H2} and σ_{H2} , using the exponentially decreasing cloud covering factor distribution (equation 6). The models shown *are not fits to the data*, but simply a close approximation of the observations. In all cases, the models have been generated with a similar dynamical range in $\text{Log}(\Sigma_{H2})$ at the $3\ \sigma$ detection limit, as used by Liu et al. (2011) for their analysis.

For M51a, the observed trends of both γ_{H2} and σ_{H2} are more closely, and simultaneously, reproduced by $\beta=1.5$ with about 1% of the SFR removed (meaning that the lowest mass clouds, $M_{\text{cloud}} \leq 10^{3.8}\ M_\odot$, that produce the bottom 1% of the star formation are assigned $\text{SFR}=0$, top panels of Figure 15). A small excess in the predicted γ_{H2} is, however, found for regions $>700\ \text{pc}$. Best fitting models for γ_{H2} with $\beta=1.0$ and 2.0 tend to produce a flat trend for region sizes $<400\ \text{pc}$; $\beta=2.0$ models also predict steeper slopes than observed at sizes $>700\ \text{pc}$. However, the main discrepancy between $\beta=1.0$ and 2.0 models and observations is in the σ_{H2} trend (Figure 15, top-right panel): both models predict larger-than-observed scatter about the best fit lines for regions $<700\ \text{pc}$. Changing parameters in the Default Model is unlikely to help improve the agreement between models and observations: parameter choices that would decrease the values of σ_{H2} (e.g., decrease in the scatter of the SFR–cloud mass relation or decrease in the SFR threshold) would also decrease the values of γ_{H2} at fixed region size, thus introducing a discrepancy between models and observations for this quantity. Using a homogeneous distribution of cloud covering factors provides similar results that only minimally differ in the quantification of the background or thresholds to implement (typically by 5%).

There is a large degree of degeneracy among the models that can reproduce the data for γ_{H2} in NGC3521 (Figure 15, bottom-left panel). Within the $1\text{--}1.5\sigma$ uncertainty of the data, the observed trend and amplitude of γ_{H2} are reproduced by: a $\beta=2.0$ model with a 25% added background to the SFR; a $\beta=1.5$ with a 10% background; and a $\beta=1.0$ with a cloud mass threshold that removes 40% of the SFR. For σ_{H2} , the $\beta=1.5$ reproduce the observed trend more accurately than the $\beta=1.0$ and $\beta=2.0$ models, although none of the models matches the data for sizes <400 pc. The high inclination of NGC3521 is likely to complicate any comparison with models.

If M51a and NGC3521 share a common underlying relation between SFR and cloud mass, we conclude that the Observed SK Law slope and data scatter can more closely be reproduced by an exponent $\beta=1.5$. In the case of M51a, Liu et al. (2011) appear to have slightly (by about 1%) over-subtracted the low-frequency background in the SFR maps, and to have slightly under-subtracted it (by about 10%) in the case of NGC3521. To test this picture, we compare the trend in γ_{H2} of both galaxies as a function of the dynamical range (expressed as a detection threshold, 1σ to 5σ , for Σ_{H2}), as derived by Liu et al. (2011). We choose two representative projected region sizes, 300 pc and 700 pc, from Tables 3 and 4 of those authors, which correspond to de-projected region sizes of 330 pc and 770 pc in M51a and 500 pc and 1200 pc in NGC3521. Figure 16 shows that the models reasonably, albeit not perfectly, reproduce the observational trends; the largest deviations ($>2\sigma$ along the vertical axis) are observed in M51a for the highest detection limits, where the slopes are systematically over-predicted by $\delta\gamma_{H2}/\gamma_{H2} \lesssim 10\%$. This disagreement is likely driven by the decreasing dynamical range of the data for increasing detection limit. However, the comparison in Figure 16 stresses the similarity in the trend as a function of detection limit for model and data, despite the numerical discrepancy.

Within the picture above, we can attempt to interpret results on the same two galaxies obtained by other authors. Among the pixel-based analyses, Bigiel et al. (2008) obtain $\gamma_{H2}=0.84$ and 0.95 for M51a and NGC3521, respectively, with $\sigma_{H2} \sim 0.2$ over region sizes $=750$ pc (could be 1 kpc for NGC3521 if the galaxy is closer than what those authors assumed, see Liu et al. 2011). Bigiel et al. (2008) use a combination of FUV and $24\mu\text{m}$ data to derive spatially-resolved SFRs, and do not remove any low-frequency background from their SFR maps, on account that both FUV and $24\mu\text{m}$ emission should be mostly tracing current SFR. The low frequency background removed by Liu et al. (2011) corresponds, as already remarked, to about 50% of the total luminosity tracing the SFR; in our models, re-adding this background to the simulations corresponds to adding a contribution equivalent to $\sim 100\%$ of the mean SFR. Bigiel et al. (2008) also analyze their data above a 3σ significance level for Σ_{H2} . Our Default Model, using $\beta=1.5$ and a uniform background contribution in the range 60%–80%, yields γ_{H2} in the range 0.90–0.81 at 750 pc and 0.85–0.76 at 1 kpc, and a scatter

about the best fit lines $\sigma_{H2} \sim 0.25$, for $\Sigma_{H2} \geq 3 \sigma$. The values of the model slopes approach the results obtained by Bigiel et al. (2008), similar to the conclusion reached by Liu et al. (2011) using observational data. Even when adopting a more modest background level of 20% of the total, as recently suggested by Leroy et al. (2012), which corresponds to 30% in our convention, the models with $\beta=1.5$ yield overall low values of γ_{H2} , in the range 1.10–1.03 for region sizes in the range 750–1,000 pc.

Still for M51a, using region sizes ~ 170 pc, Blanc et al. (2009) derive a slope $\gamma_{H2}=0.82 \pm 0.05$ and a scatter about the mean trend $\sigma_{H2}=0.43 \pm 0.02$. Blanc et al. (2009) use the extinction–corrected $H\alpha$ emission to trace the SFR, and remove a uniform background at the level of 11% of the total $H\alpha$, on the basis that the diffuse $H\alpha$ component may be due to contributions from adjacent regions, and, therefore, not measure the local SFR. These authors fit their data including upper limits to both the molecular gas and SFR surface density components. We attempt to reproduce this scenario with our Default Model, by adopting a 50%–60% contribution from a uniform background (10%–20% less than in the case of Bigiel et al. 2008, to simulate the background removal of Blanc et al. (2009)), $\beta=1.5$, same region sizes as Blanc et al. (2009), and no detection limit to Σ_{H2} (see Figure 9). Our simulations yield $\gamma_{H2}=0.85$ – 0.80 for the two background choices, and $\sigma_{H2} \sim 0.32$. Varying the fraction of background added to the SFR can lead to better or worse agreement with the observational data. Finally, the results by Kennicutt et al. (2007), where a slope of 1.37 is obtained for the molecular SK Law, are difficult to interpret within the framework of our simulations, as those authors center their 500 pc apertures on peaks of star formation.

Independently of the exact details of each measure, the wealth of independent measures for M51a offers the opportunity to investigate some trends that should be applicable to galaxies in general. The steep slopes obtained by Liu et al. (2011) can be reconciled with the much shallower slopes obtained by Bigiel et al. (2008) and Blanc et al. (2009) if: the relation between SFR and cloud mass is super–linear, specifically $\beta \sim 1.5$; a uniform background at the level of $\approx 60\%$ – 80% of the SFR (i.e., 30%–40% of the galaxy luminosity) is present in the SFR maps of Bigiel et al. (2008) and Blanc et al. (2009); a slight over–removal (by about 1% of the SFR) of this background is present in the SFR data of Liu et al. (2011). This scenario can also account for the trend in σ_{H2} at fixed region size; at 750 pc, it decreases from a value ~ 0.45 (Liu et al. 2011) to ~ 0.2 (Bigiel et al. 2008) (and from ~ 0.44 to 0.25 in our models), if a uniform contribution to the SFR is present in the measurements from the latter authors. Finally, while the slope measured by Blanc et al. (2009) is similar to that of Bigiel et al. (2008), their scatter is about a factor of 2 larger; the shallow slope in Blanc et al. (2009) is likely a combination of residual background in the SFR maps, together with the use of low significance data in their fits; the large scatter σ_{H2} in Blanc et al. (2009) reflects the impact of stochastic sampling of the molecular cloud mass function in their small regions (170 pc in

size versus 750-1,000 pc of Bigiel et al. 2008).

6.2.2. Other Galaxies

We can attempt to interpret other results within this scenario. One of the best studied galaxies in this regard is our neighbor M33 (Wong & Blitz 2002; Heyer et al. 2004; Verley et al. 2010; Onodera et al. 2010), which, at only 840 kpc distance and with modest inclination (54°), offers one of the most unimpeded views of star formation in an external spiral galaxy. We concentrate on the results of Verley et al. (2010), who perform both azimuthally averaged and spatially resolved analyses, in addition to discriminate between OLS and least square fitting techniques. Verley et al. (2010) attempt to account for the contamination of the SFR maps from an unrelated diffuse emission in the infrared (at the level of 30%), and use data above 2σ significance. We compare the results from Verley et al. (2010) to our Default Model with $\log[M_{\text{cloud}}(\text{max})]=6.5$, to approach the actual situation in M33, where molecular clouds have maximum masses around $10^6 M_\odot$ (Engargiola et al. 2003). Our $\beta=1.5$ simulation of azimuthally-averaged bins, with maximum radius of 6 kpc and radial step of 240 pc, as adopted by Verley et al. (2010) for their data, yields $\gamma_{H2}=1.30\pm0.10$, when using the bi-linear regression fit routine FITEXY, to be compared with the observed value $\gamma_{H2}=1.1\pm0.1$. Heyer et al. (2004) obtain a larger value for $\gamma_{H2}=1.36\pm0.08$, more similar to our model results. These authors do not remove a low frequency background and should, in principle, obtain a shallower slope than that of Verley et al. (2010). Their steeper slope could be partly due to an insufficient accounting of the unobscured SFR, since the authors trace the SFR with infrared emission only. The direct correlation between intensity of the star formation and dust attenuation (e.g., Calzetti et al. 2007) gives larger weight to the brighter star-forming regions when infrared SFR tracers are used, and yields a steeper SK Law, while use of UV and/or optical (i.e. subject to dust attenuation) SFR tracers will yield shallower-than-expected SK Laws. Within this framework, we can easily interpret Wong & Blitz (2002)’s results, which use $H\alpha$ as a SFR tracer and obtain steeper slopes when galactocentric-dependent dust attenuation corrections are applied to the SFR data.

For the spatially resolved analysis, Verley et al. (2010) adopt a scale of 180 pc, and use both FITEXY and the OLS bi-sector fitting, obtaining $\gamma_{H2}=2.22\pm0.07$ and 1.46 ± 0.34 , respectively; these are to be compared with our simulation’s $\gamma_{H2}=2.47\pm0.18$ and 1.61 ± 0.02 , respectively, and $\sigma_{H2}=0.43$. Onodera et al. (2010) derive a slope $\gamma_{H2}=1.18\pm0.11$, on scales of 1 kpc, using a 2σ detection limit for the data and a least-square fit routine. They do not remove a low-frequency background from their SFR data. Assuming a background level similar to that determined by Verley et al. (2010) (corresponding to 60% background level

in our convention), we determine $\gamma_{H_2}=0.99\pm0.08$ for M33 at 1 kpc scale using our bi-linear regression fit routine, in good agreement with the value from Onodera et al. (2010). In general, our Default Model, adapted to the smaller clouds in M33, reproduces the observed trends in the SK Law slope fairly well, and the actual γ_{H_2} typically within 1–2 σ uncertainties, for $\beta=1.5$.

Thilker et al. (2007) perform a pixel-based analysis of NGC7331, a highly inclined galaxy (77°) at a distance of 14.7 Mpc. The authors' $6''$ bins correspond, once projection effects are removed, to areas with ~ 900 pc size. The authors also separate between regions dominated by H_2 and regions dominated by HI; the two regimes are distinguished by the H_2 -dominated regime having $\text{Log}(\Sigma_{H_2}) \gtrsim 0.8$ and the HI-dominated regime characterized by $\text{Log}(\Sigma_{H_2}) \lesssim 1.1$. For the first regime, a plot of Σ_{SFR} versus Σ_{H_2} gives a slope of 1.64, while in the second case the authors recover a shallower slope, $\gamma_{H_2}=1.20$, thus yielding a difference in slope of $\Delta\gamma_{H_2} \sim 0.45$. Using $\beta=1.5$ and dividing the simulations into two regimes at $\text{Log}(\Sigma_{H_2})=0.9$, we get $\gamma_{H_2}=1.58$ for the high Σ_{H_2} range and $\gamma_{H_2}=1.16$ for the low Σ_{H_2} range, with $\Delta\gamma_{H_2} \sim 0.4$, similar to that derived by Thilker et al. (2007).

Rahman et al. (2011) present a pixel-based analysis for a sample of 14 nearby star-forming late-type spirals, using interferometry CARMA data for the molecular gas, with 1 σ detection limit around $3 M_\odot \text{ pc}^{-2}$, and the 24 μm emission to trace the SFR. To avoid potential contamination from low-surface-brightness quiescent regions, they limit their analysis to pixels with gas surface density $\Sigma_{H_2} \geq 20 M_\odot \text{ pc}^{-2}$. Analysis using both pixels at native resolution ($6''$) and at common 1 kpc resolution yield an overall slope $\gamma_{H_2} \sim 1.1 \pm 0.1$ and a galaxy-average slope $\gamma_{H_2} = 0.96 \pm 0.16$ (OLS bisector fit). We use the best fit model for M51a, which includes a 80% background contribution, simulated at 1 kpc region size to compare with the results of Rahman et al. (2011); for $\log(\Sigma_{H_2}) \geq 1.3$, we find $\gamma_{H_2}=1.10$, with $\sigma_{H_2}=0.22$. When combining simulations in a range of region sizes between 200 pc and 1,000 pc, to approximate the authors' analysis at fixed angular resolution of $6''$, we obtain $\gamma_{H_2}=1.21$. Thus, despite the unavoidable variations from galaxy to galaxy, the model used to account for the observational results of M51a can be effectively applied to other late-type spirals. Our result also indicates that restricting analyses to molecular gas surface brightnesses $\Sigma_{H_2} \geq 20 M_\odot \text{ pc}^{-2}$ is not completely effective at avoiding the influence of a diffuse background contribution to the SFR, because of the potentially large background levels. Higher thresholds for Σ_{H_2} may, conversely, excessively restrict the dynamical range in gas surface density, thus decreasing the fidelity of the fitted relations.

In conclusion, when we have sufficient information on the observational conditions to implement those conditions in our simulations, we tend to reproduce both the power law exponent and scatter about the mean of the Observed SK Law, using as a starting point a

common relation between SFR and cloud mass.

6.3. Limitations

Although our simple model can account for some of the trends observed in recent data analyses of the SK Law, it contains a number of simplifications that will limit its applicability. For instance, in the previous section, we remarked that SK Law analyses involving specific selection criteria for the sub-galactic regions, used in lieu of blind pixellation, cannot be reproduced by our simulations.

The most notable limitation, however, is the *constant scaling* adopted for all simulations sharing the same relation between SFR and M_{cloud} . Thus, we cannot account for situations where the scaling of gas-to-stars conversion changes. This includes the ‘global’ SK Law, i.e., the relation between the SFR and gas surface densities for whole galaxies, where the observed trend, either as a progressive (Kennicutt 1998) or sudden (Daddi et al. 2010; Genzel et al. 2010) change in the relation between the two quantities, has been interpreted in terms of a change in the star formation efficiency (SFE) as the total SFR surface density increases from normal disks to starburst galaxies.

The constant scaling can also affect the comparison between simulations and observations for azimuthally averaged studies, if the SFE changes among substructures within galaxies (Momose et al. 2010), and/or is higher in the center than in the outer regions (e.g., the galaxy hosts a central starburst). It should be remarked, however, that there is a degeneracy between changes in SFE and a non-linear relation between SFR and M_{cloud} . For instance, a low SFE in interarm regions may be simply the result of these regions hosting small clouds, unlike their spiral arm counterparts (e.g. Koda et al. 2009); this situation is simulated in our models through variations in the covering factor of regions. The resolution of the degeneracy between the two potential interpretations (increase in SFE versus variations in the clouds’ maximum mass in different environments) will require resolving structures in galaxies at the molecular cloud scale (e.g., with ALMA).

Our models do not include a direct connection between SFR and dense gas (Heiderman et al. 2010; Lada, Lombardi & Alves 2010). We use a very simplified and ad-hoc model for the relation between SFR and relatively low density gas ($n \sim 10^2 \text{ cm}^{-3}$, as traced by low-J ^{12}CO). Within this scenario, a linear relation between SFR and high density gas could imply a non-linear correlation between low and high density gas. Recent investigations on a few molecular clouds in proximity of the Sun give contrasting results (Gutermuth et al. 2011; Lada et al. 2010), highlighting the need for more extensive analyses.

Finally, we do not model in detail any physical displacement between recent star formation and peaks of cold gas emission, which is, however, observed in many galaxies (e.g., Kennicutt et al. 2007; Momose et al. 2010). This displacement will affect results at the smallest region sizes, and may be a partial cause for the large scatter observed in the data of Blanc et al. (2009). However, we mitigate the absence of a displacement component in the models by assigning a scatter to the SFR–cloud mass relation, which allows for the existence of clouds with much lower and much higher SFR than the mean.

7. Summary and Conclusions

In an attempt to understand the large variety of results on the Observed (molecular) SK Law reported in the literature, we have simulated spatially–resolved galaxies using simple recipes for the relation between SFR and cloud mass, the cloud mass and radius, and the cloud mass function. We have added reasonable sources of scatter, such as a random covering factor for each region (uniformly or exponentially distributed), gaussian scatter between the cloud mass and radius and between the SFR and cloud mass, and detection noise in Σ_{H_2} . We have then proceeded to investigate the slope γ_{H_2} and scatter about the best fit line, σ_{H_2} of the Observed SK Law.

Our main result is that the Observed molecular SK Law, which relates the surface densities of cold gas and SFR, is a complex convolution of the intrinsic relation between SFR and gas clouds with stochastic sampling of the cloud mass function, and strongly depends on the region size considered. Its dynamical range, slope, and scatter about the mean trend are affected by the scatter between cloud mass and radius, between SFR and cloud mass, and by the dynamical range and sensitivity of the cold gas data. The slope γ_{H_2} is also a function of the fitting method adopted (Figure 7), as already noted by Blanc et al. (2009) and Verley et al. (2010).

The scatter about the mean trend, σ_{H_2} , is a sensitive function of the measurement uncertainties in Σ_{H_2} , and of the slope and scatter in the SFR– M_{H_2} relation. For a slope $\beta=1.0$ between SFR and M_{H_2} , and in the absence of scatter between these two quantities, the scatter σ_{H_2} about the mean trend of the SK Law is dominated by the sensitivity of the cold gas map coupled with the non–symmetric nature of error bars in logarithmic scale. As β increases, also σ_{H_2} increases: at constant region size <1 kpc, σ_{H_2} roughly triples and quadruples for $\beta=1.5$ and 2.0 , respectively, relative to the $\beta=1.0$ value. This increase of σ_{H_2} for increasing β reflects the combination of the non–linear relation between SFR and M_{H_2} and stochastic sampling of the cloud mass function at small region sizes. Introducing a scatter between SFR and M_{H_2} has the general (and expected) effect of increasing σ_{H_2} at

all β values.

The presence of a large contribution to σ_{H2} from the typically shallow sensitivity limit of the cold gas maps argues in favor of pursuing deep CO imaging of nearby galaxies to improve their sensitivity and increase the dynamical range probed. Significant improvements have been brought by CO mapping with the Nobeyama 45-m millimeter telescope (e.g., Momose et al. 2010; Liu et al. 2011), and more will be ushered by the Large Millimeter Telescope and other large single-dish facilities. More sensitive maps than currently available will break the degeneracy among the various contributors to the scatter σ_{H2} .

For $\text{SFR} \propto M_{H2}^\beta$ and $\beta > 1.0$, the slope of the Observed SK Law $\gamma_{H2} \neq \beta$, and the SK Law slope is in general a decreasing function of the region size. At small region sizes, typically $< 400\text{--}500$ pc, $\gamma_{H2} > \beta$, and at large region sizes, > 700 pc–1 kpc, $\gamma_{H2} \lesssim \beta$. As the region size increases, γ_{H2} tends to unity, a reflection of the increasing ability of the larger regions to sample the cloud mass function reliably. These general trends with region size persist for a large range of parameter variations, including cloud mass function slope and maximum cloud mass, cloud covering factor distribution, and variation in the scatter between SFR and M_{H2} . They also persist when changing sensitivity limits and dynamical range for the cold gas maps (Figures 8 and 9), and the fitting method. While we model our ‘galaxies’ as single cloud layers (areal covering with thickness=1 cloud), moving to multiple clouds along the line of sight (volume filling) has the general effect of further flattening γ_{H2} towards values of unity, irrespective of β and region size.

The general absence of a 1-to-1 relation between γ_{H2} and β poses a challenge for studies of the SK Law on sub-galactic scales. In this respect, it becomes important that spatially-resolved studies, but which cannot resolve individual clouds, investigate trends as a function of region size. Furthermore, the fact that γ_{H2} converges to unity for large region sizes, virtually irrespective of any condition, strongly argues against the approach of using kpc-size or larger regions to derive the SK Law, unless these sizes are part of a thorough investigation that includes a range of sub-kpc region sizes.

The case of $\beta=1.0$ provides the most stable condition for γ_{H2} which remains close to β , within $\pm 0.1/0.2$, for a large range of parameters. The most notable exceptions are the cases where: (i) a large scatter is present between SFR and M_{H2} (Figure 5, bottom-left); and (ii) a large threshold has been applied to the SFR tracers (Figure 12, left). In both cases, large (>1) values of γ_{H2} are accompanied by large values of the scatter σ_{H2} about the mean trend. The case of a SFR threshold is easier to control, as it is produced at the level of data handling; an artificial threshold, for instance, implies that a fraction of regions do not contain detectable SFR. As an example, if 60% of the SFR at the low end is removed, about 70% of the 200 pc regions and about 50% of the 300 pc regions do not contain detectable

star formation. In this respect, if SFR is linked to the cloud mass via a linear relation, measurements of the Observed SK Law will yield in general values close to unity. Deviations from this value should indicate a power-law index $\beta > 1$.

We have compared our simulations against the Observed SK Law for three nearby galaxies, M51a, M33, and NGC3521, for which we have been able to reconstruct the assumptions that have entered into the analysis of the data by the original authors. In all cases, we have been able to reproduce, within $1\text{--}2\sigma$, the measured slopes and the observed scatter about the mean trend using a common relation between SFR and M_{H2} with $\beta=1.5$. The large range of values, especially for γ_{H2} , obtained by different authors are a manifestation of different regions sizes, detection thresholds, fitting methods, and treatments of the background contamination that affects the emission used to trace SFRs. Current data, especially for the two low-inclination galaxies M51a and M33, do not support $\beta=1.0$ as the exponent linking SFR and cloud mass. However, a more extensive set of observations and analyses will be needed to place this conclusion on a firmer footing.

We have also established that including data on the cold gas below a $2\text{--}3\sigma$ threshold causes a flattening of γ_{H2} that can result in $\gamma_{H2} < \beta$ (Figure 9), implying that care should be taken when including low significance data in analyses of the SK Law, as already remarked by Verley et al. (2010).

Presence of a background unrelated to current star formation in the maps used to trace SFR will generally cause a flattening of γ_{H2} relative to β . Presence of a threshold in SFR, for which the least massive clouds do not form stars, will have as general effect a steepening of γ_{H2} . Hence, a detailed understanding of the contributors to a specific band used to trace SFR will be crucial for pinning down the relation between SFR and cold gas. While there is likely general agreement that backgrounds exist, there is still controversy on what fraction of the total emission in a galaxy this background represents, and how it is distributed. Clearly, this represents a fundamental and necessary step to perform in order to unravel the functional form of the scaling law of star formation, and the combination of trends in γ_{H2} and σ_{H2} can provide valuable discriminators.

In summary, disentangling the physical relation linking star formation to gas clouds from observational and analysis imprints will require that future studies derive the SK Law, its slope and scatter about the mean trend, using a range of physical sizes within each galaxy, and that the sensitivity limit and dynamical range of the cold gas data and other conditions in the analysis are carefully taken into account as a source of bias for both γ_{H2} and σ_{H2} .

This work has been partially supported by the NASA ADP grant NNX10AD08G.

REFERENCES

- Bigiel, F., Walter, F., Leroy, A., Brinks, E., de Block, W.J.D., Madore, B., & Thornley, M.D. 2008, *AJ*, 136, 2846
- Bigiel, F., Leroy, A.K., Walter, F., Brinks, E., de Block, W.J.D., Kramer, C., Rix, H.W., Schrubba, A., Schuster, K.-F., Usero, A., & Wiese Meyer, H.W. 2011, *ApJ*, 730, L13
- Blanc, G.A., Heiderman, A., Gebhardt, K., Evans, N.J., & Adams, J. 2009, *ApJ*, 704, 842
- Blitz, L., & Rosolowsky, E. 2004, in *IMF50: The Initial Mass Function 50 Years Later*, eds. E. Corbelli, F. Palla, & H. Zinnecker, 287
- Blitz, L., Fukui, Y., Kawamura, A., Leroy, A., Mizuno, N., & Rosolowsky, E. 2007, in *Protostars and Planets V*, ed. B. Reipurth, D. Jewitt, & K. Keil, 81
- Boissier, S., Prantzos, N., Boselli, A., & Gavazzi, G. 2003, *MNRAS*, 346, 1215
- Bolatto, A.D., Leroy, A.K., Rosolowsky, E., Walter, F., & Blitz, L. 2008, *ApJ*, 686, 948
- Calzetti, D., Kennicutt, R.C., Engelbracht, C.W., Leitherer, C., Draine, B.T., Kewley, L., Moustakas, J., Sosey, M., Dale, D.A., Gordon, K.D., et al. 2007, *ApJ*, 666, 870
- Calzetti, D., Chandar, R., Lee, J.C., Elmegreen, B.G., Kennicutt, R.C., & Whitmore, B. 2010, *ApJ*, 719, L158
- Corbelli, E., Verley, S., Elmegreen, B.G., & Giovanardi, C. 2009, *A&A*, 495, 479
- Daddi, E., Elbaz, D., Walter, F., Bournaud, F., Salmi, F., Carilli, C., Dannerbauret, H., Dickinson, M., Monaco, P., & Riechers, D. 2010, *ApJ*, 714, L118
- Dobbs, C.L., Burkert, A., & Pringle, J.E. 2011, *MNRAS*, in press (astro-ph/1107.0154)
- Elmegreen, B.G. 1989, *ApJ*, 342, 67
- Elmegreen, B.G. 1994, *ApJ*, 433, 39
- Elmegreen, B.G. 2002, *ApJ*, 577, 206
- Elmegreen, B.G. 2007, *ApJ*, 668, 1064
- Engargiola, G., Plambeck, R. L., Rosolowsky, E., & Blitz, L. 2003, *ApJS*, 149, 343
- Enoch, M.L., Glenn, J., Evans, N.J., Sargent, A.I., Young, K.E., & Huard, T.L. 2007, *ApJ*, 666, 982

- Feldmann, R., Gnedin, N.Y., & Karvtsov, A.V. 2011, *ApJ*, 732, 115
- Fukui, Y., & Kawamura, A. 2010, *ARA&A*, 48, 547
- Gao, Y., & Solomon, P.M. 2004, *ApJ*, 606, 271
- Genzel, R., Tacconi, L.J., Gracia-Carpio, J., Sternberg, A., Cooper, M.C., Shapiro, K., Bolatto, A., Bouchè, N., Bournaud, F., Burkert, A., et al. 2010, *MNRAS*, 407, 2091
- Gratier, P., Braine, J., Rodriguez-Fernandez, N.J., Schuster, K.F., Kramer, C., Corbelli, E., Combes, F., Brouillet, N., van der Werf, P.P., & Röllig, M. 2011, *A&A*, in press (astroph/1111.4320)
- Gutermuth, R.A., Pipher, J.L., Megeath, S.T., Myers, P.C., Allen, L.E., & Allen, T.S. 2011, *ApJ*, in press (astroph/1107.0966)
- Hartmann, L., Ballesteros-Paredes, J., Bergin, E.A. 2001, *ApJ*, 562, 852
- Heiderman, A., Evans, N., Allen, L.E., Huard, T., & Heyer, M. 2010, *ApJ*, 723, 1019
- Heyer, M.H., Carpenter, J.M., & Snell, R.L. 2001, *ApJ*, 551, 852
- Heyer, M.H., Corbelli, E., Schneider, S.E., & Young, J.S. 2004, *ApJ*, 602, 723
- Heyer, M.H., Krawczyk, C., Duval, J., & Jacksonm, J.M. 2009, *ApJ*, 699, 1092
- Isobe, T., Feigelson, E.D., Akritas, M.G., & Babu, G.J. 1990, *ApJ*, 364, 104
- Juneau, S., Narayanan, D.T., Moustakas, J., Shirley, Y.L., Bussmann, R.S., Kennicutt, R.C., & Vanden Bout, P.A. 2009, *ApJ*, 707, 1217
- Kawamura, A., Mizuno, Y., Minamidani, T., et al. 2009, *ApJS*, 184, 2009
- Kennicutt, R.C. 1989, *ApJ*, 344, 685
- Kennicutt, R.C. Jr. 1998, *ApJ*, 498, 541
- Kennicutt, R.C., Calzetti, D., Walter, F., Helou, G.,m Hollenbach, D., Armus, L., Bendo, G., Dale, D.A., Draine, B.T., Engelbracht, C.W., et al. 2007, *ApJ*, 671, 333
- Koda, J., Scoville, N., Sawada, T., La Vigne, M.A., Vogel, S.N., Potts, A.E., Carpenter, J.M., Corder, S.A., Wright, M.C.H., White, S.M., et al. 2009, *ApJ*, 700, L132
- Kroupa, P. 2001, *MNRAS*, 322, 231

- Krumholz, M.R., & McKee, C.F. 2005, *ApJ*, 630, 250
- Krumholz, M.R., McKee, C.F., & Tumlinson, J. 2009, *ApJ*, 699, 850
- Lada, C.J., Lombardi, M., & Alves, J.F. 2010, *ApJ*, 724, 687
- Lada, C.J., Forbrich, J., Lombardi, M., & Alves, J.F. 2011, *ApJ*, in press (astroph/1112.4466)
- Larson, R.B. 1981, *MNRAS*, 194, 809
- Lee, Janice C., Gil de Paz, A., Tremonti, C., Kennicutt, R.C., Salim, S., Bothwell, M., Calzetti, D., Dalcanton, J., Dale, D., Engelbracht, C., et al. 2009, *ApJ*, 706, 599
- Lee, Janice C., Gil de Paz, A., Kennicutt, R.C., Bothwell, M., Dalcanton, J., Funes, J.G.S., Johnson, B.D., Sakai, S., Skillman, E., Tremonti, C., & van Zee, L. 2011, *ApJS*, 192, 6
- Leroy, A.K., Walter, F., Brinks, E., Bigiel, F., de Blok, W. J. G., Madore, B., & Thornley, M. D. 2008, *AJ*, 136, 2782
- Leroy, A.K. Walter, F., Bigiel, F., Usero, A., Weiss, A., Brinks, E., De Blok, W.J.G., Kennicutt, R.C., Schuster, K.-F., Kramer, C., Wiesenmeyer, H.W., & Roussel, H. 2009, *AJ*, 137, 4670
- Leroy, A.K. , Bigiel, F., de Blok, W.J.G., Boissier, S., Bolatto, A., Brinks, E., Madore, B., Munoz–Mateos, J.-C., Murphy, E., Sandstrom, K., et al. 2012, *AJ*, in press (astroph/1202.2873)
- Liu, G., Koda, J., Calzetti, D., Fukuhara, M., & Momose, R., 2011, *ApJ*, 735, 63
- Mac Low, M.-M., & Klessen, R.S. 2004, *RvMP*, 76, 125
- , Madore, B.F. 1977, *MNRAS*, 178, 1
- Mizuno, N., Yamaguchi, R., Mizuno, A., Rubio, M., Abe, R., Saito, H., Onishi, T., Yonekura, Y., Yamaguchi, N., Ogawa, H., & Fukui, Y. 2001, *PASJ*, 53, 971
- Momose, R., Okumura, S.K., Koda, J., & Sawada, T. 2010, *ApJ*, 721, 383
- Monaco, P., Murante, G., Borgani, S., & Dolag, K. 2011, *MNRAS*, in press (astroph/1109.0484)
- Narayanan, D., Cox, T.J., Shirley, Y., Dave, R., Hernquist, L., & Walker, C.K. 2008, *ApJ*, 684, 996

- Onodera, S., et al. 2010, ApJ, 722, L127
- Press, W.H., Teukolsky, S.A., Vetterling, W.T., & Flannery, B.P. 2007, *Numerical Recipes: The Art of Scientific Computing*, (Cambridge University Press: Cambridge, UK)
- Rahman, N., Bolatto, A.D., Xue, R., Wong, T., Leroy, A.K., Walter, F., Bigiel, F., Rosolowsky, E., Fisher, D.B., Vogel, S.N., et al. 2011, ApJ, in press (astro-ph/1110.1630)
- Rosolowsky, E. 2005, PASP, 117, 1403
- Rosolowsky, E. 2007, ApJ, 654, 240
- Rosolowsky, E., Engargiola, G., Plambeck, R., & Blitz, L. 2003, ApJ, 599, 258
- Rownd, B.K., & Young, J.S. 1999, ApJ, 118, 670
- Schmidt, M. 1959, ApJ, 129, 243
- Schruba, A., Leroy, A.K., Walter, F., Sandstrom, K., & Rosolowsky, E. 2010, ApJ, 722, 1699
- Scoville, N.Z., Sanders, D.B., & Clemens, D.P. 1986, ApJ, 310, L77
- Scoville, N.Z., & Sanders, D.B. 1987, ASSL, 134, 21
- Scoville, N.Z., & Wilson, C.D. 2004, ASPC, 322, 245
- Silk, J. 1997, ApJ, 481, 703
- Solomon, P.M., Rivolo, A.R., Barrett, J., & Yahil, A. 1987, ApJ, 319, 730
- Tan, J.C. 2000, ApJ, 536, 173
- Tan, J.C. 2010, ApJ, 710, L88
- Thilker, D.A., Boissier, S., Bianchi, L., Calzetti, D., Boselli, A., Dale, D.A., Seibert, M., Braun R., Burgarella, D., Gil de Paz, A., et al. 2007, ApJS, 173, 572
- Verley, S., Corbelli, E., Giovanardi, C., & Hunt, L.K. 2010, A&A, 510, A64
- Villaverde, M., Cerviño, M., & Luridiana, V. 2010, A&A, 522, 49
- Weidner, C. & Kroupa, P. 2006, MNRAS, 365, 1333
- Wilson, C.D., & Scoville, N.Z. 1990, ApJ, 363, 435

Wong, T., & Blitz, L. 2002, ApJ, 569, 157

Wong, T., Hughes, A., Ott, J., Muller, E., Pineda, J.L., Bernard, J.-P., Chu, Y.-H., Fukui, Y., Gruendl, R.A., Henkel, C., et al. 2011, ApJS, in press (astro-ph/1108.5715)

Wyse, R.F.G., & Silk, J. 1989, ApJ, 339, 700

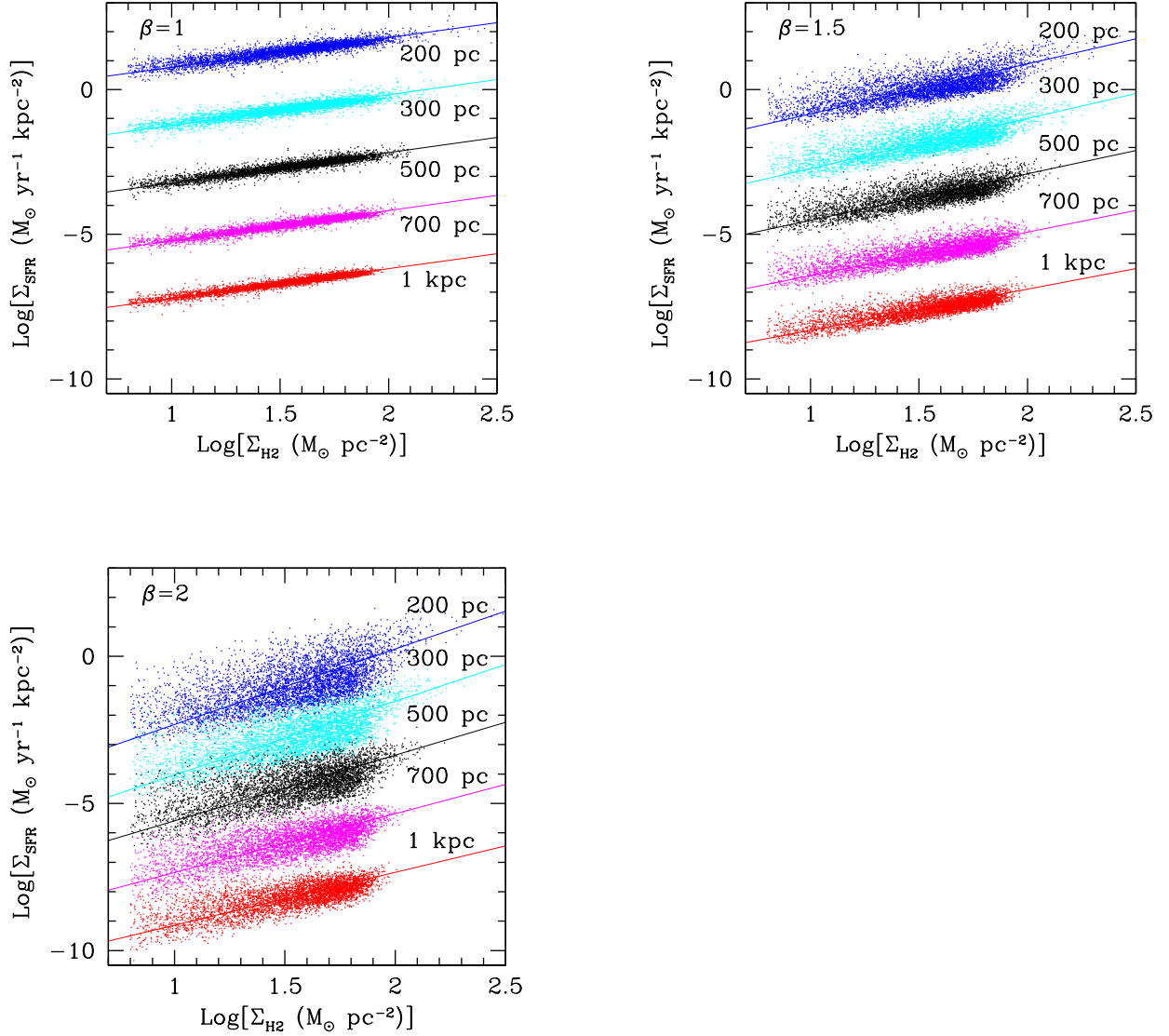


Fig. 1.— The Observed SK Law, i.e., the scaling relation between the SFR surface density and the molecular gas surface density, for the Default Model (section 2) with a uniform distribution of cloud covering factors, and three choices for the parameter β (top left of each panel) that relates SFR and cloud mass: $\text{SFR} \propto M_{\text{H}_2}^\beta$ (equation 5). ‘Data’ from the simulations (color points) and OLS bi-sector linear best fits through the simulation results (color lines) are reported for a range of linear sizes of the regions used to calculate surface densities (indicated at the right-hand-side of each simulated dataset). The 300 pc simulations (cyan) are shown at the original scale; the other datasets are shown shifted by +2 (200 pc, blue), -2 (500 pc, black), -4 (700 pc, magenta), and -6 (1 kpc, red) along the vertical direction.

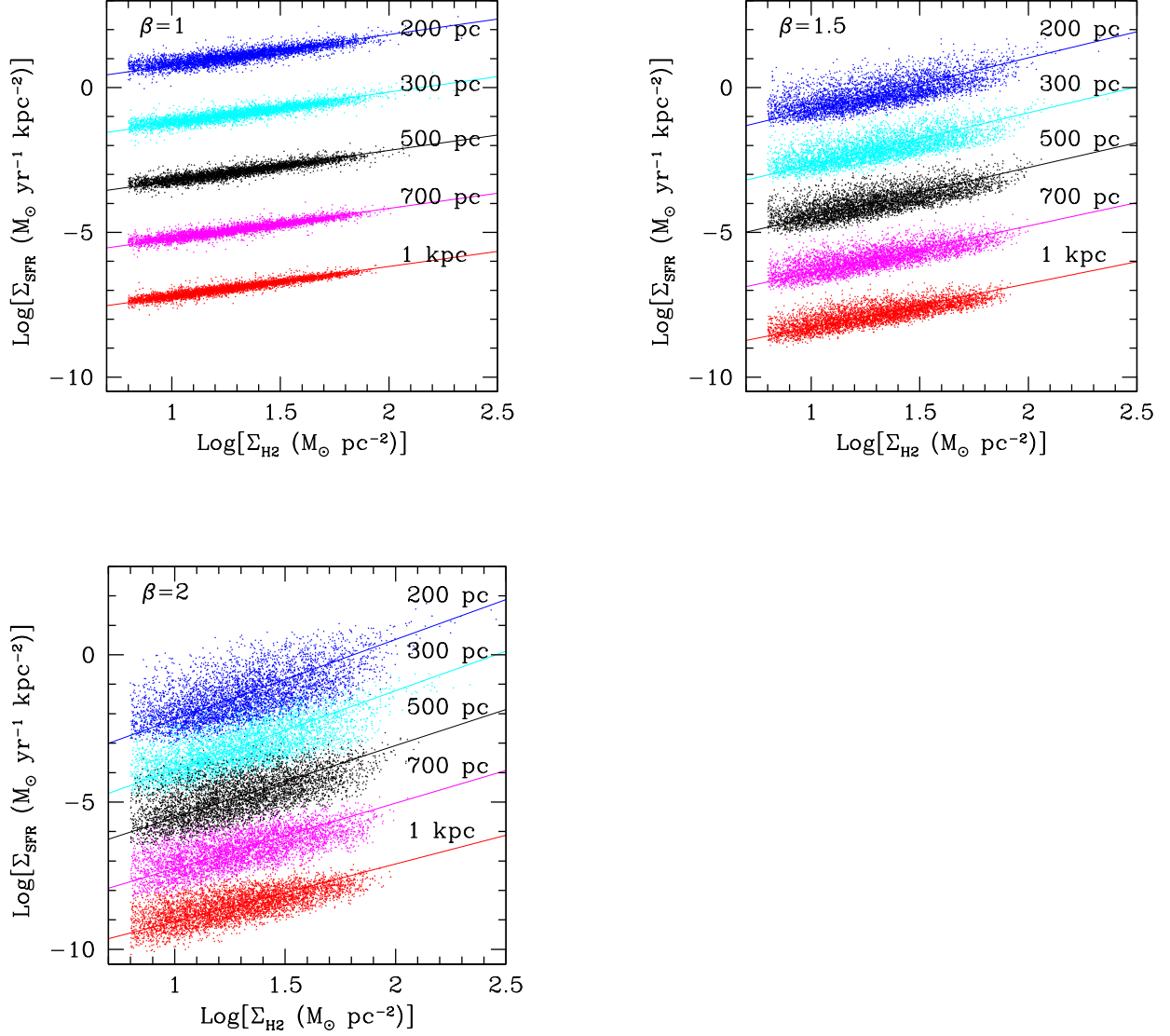


Fig. 2.— The same as Figure 1, but for an exponentially decreasing distribution of cloud covering factors (equation 6). The region at low gas surface densities is better populated by the simulated points for this covering factor distribution than in the case of a uniform distribution.

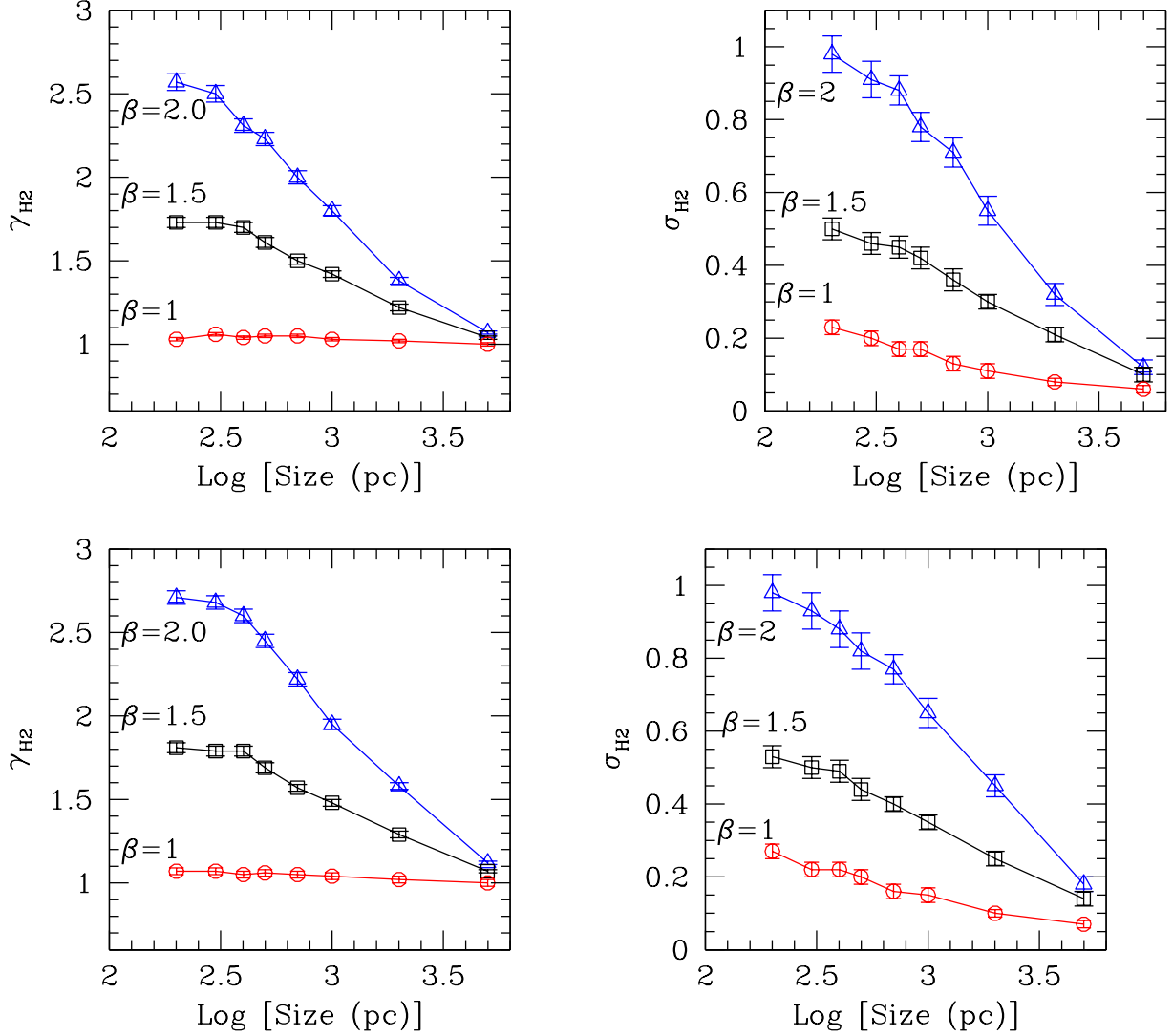


Fig. 3.— The best fit slope γ_{H_2} (left panels) and dispersion σ_{H_2} about the best fitting line (right panels) of the Observed SK Law (equation 2) for our simulations with Default Model parameters and either a uniform distribution of cloud covering factors (top panels) or an exponentially decreasing distribution of cloud covering factors (equation 6, bottom panels). All quantities are shown as a function of the sampling region’s size, in the range 200–5000 pc. The symbols connected by lines refer to: $\beta=2$ (blue triangles), $\beta=1.5$ (black squares), and $\beta=1$ (red circles), from equation 5. The measured exponents γ_{H_2} and dispersions σ_{H_2} are slightly larger in value, by ~ 0.04 – 0.14 ($\leq 6\%$), for the case of exponentially decreasing cloud covering factors than for a uniform distribution.

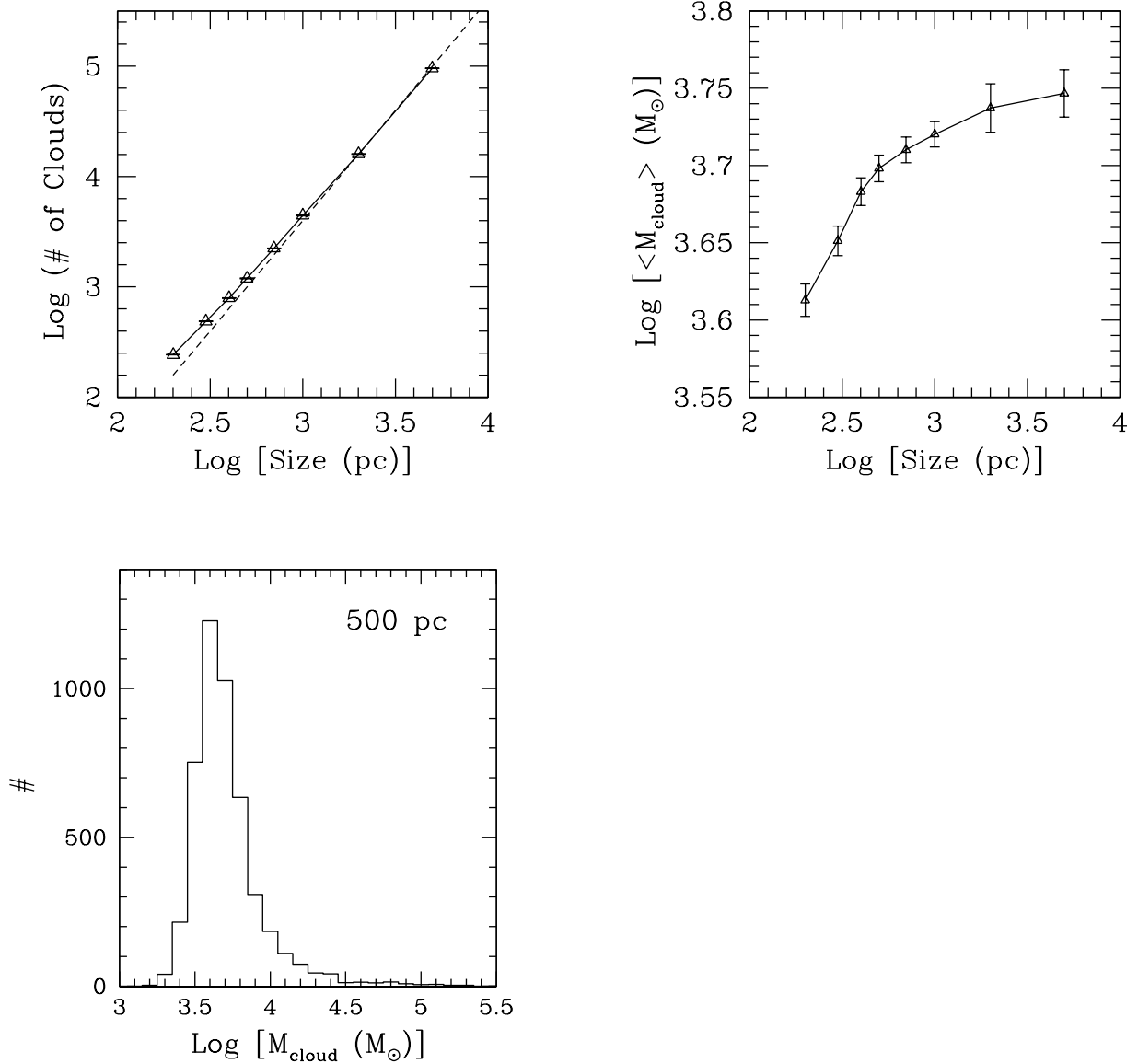


Fig. 4.— The mean number of clouds in each regions (top-left panel) and the mean cloud mass (top-right panel) as function of region size, for the Default Model with an exponential distribution of cloud covering factors. The mean number of clouds slightly (by 50% or less) exceeds the locus (dash line) expected if the mean number of clouds grows proportionally to the region’s area, up to sizes of $\sim 1\text{--}2$ kpc. The mean cloud mass flattens only beyond this region size. Both plots suggest that the cloud mass function is not fully sampled until about $1\text{--}2$ kpc. The peak of the distribution of cloud masses within the 500 pc region (bottom-left panel) is very close in value to the mean cloud mass plotted in the top-right panel. Similar plots are obtained for a uniform distribution of cloud covering factors.

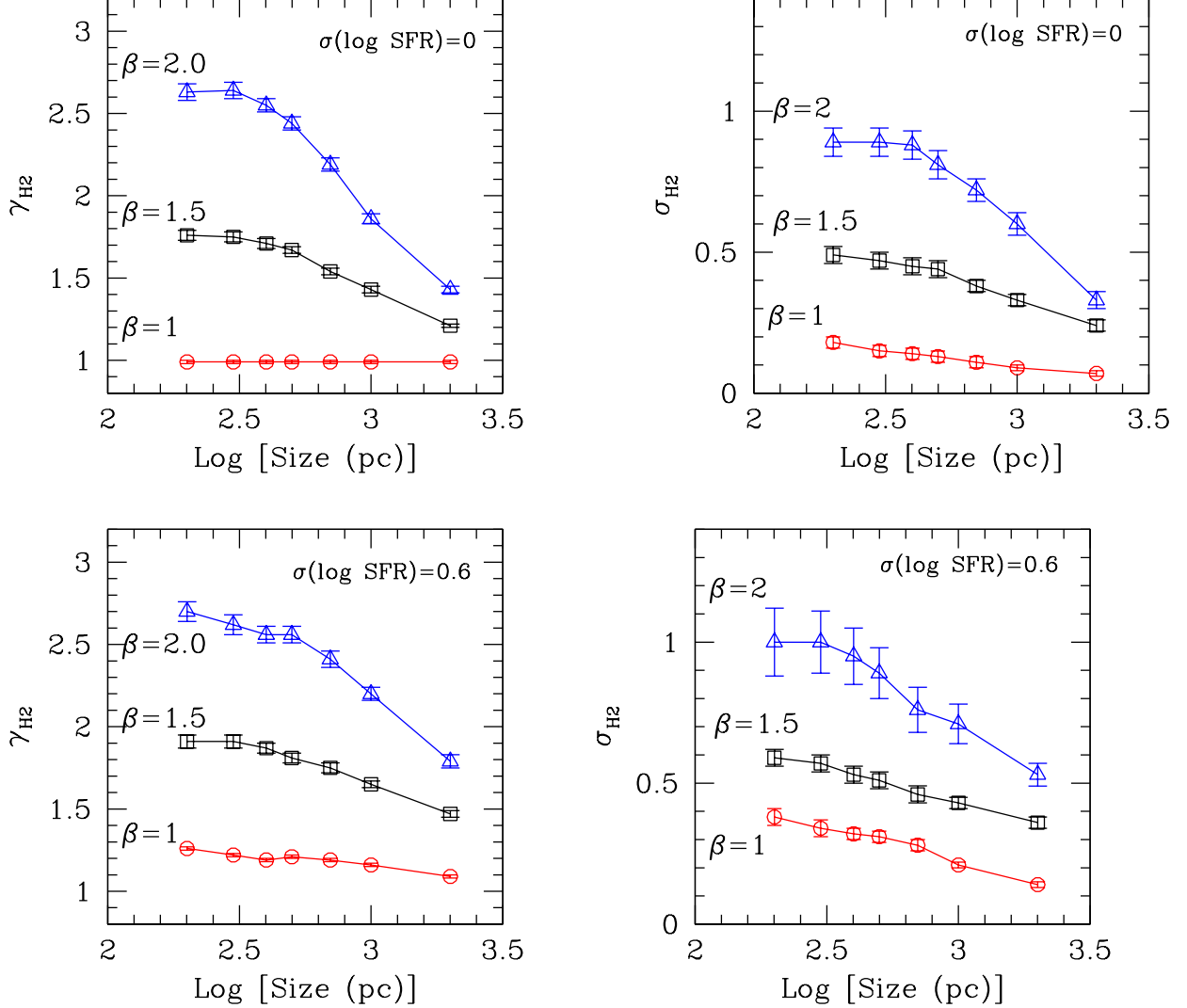


Fig. 5.— The same as Figure 3, bottom panels (exponential distribution of cloud covering factors), for the two cases in which the SFR is deterministically related to the cloud mass ($\sigma(\log \text{SFR})=0$, upper panels) and the SFR varies by a factor up to 4 (1σ , lower panels) at fixed cloud mass. The latter case is a factor of 2 larger scatter in SFR than our Default Model. Both the measured slope γ_{H_2} (left panels) and the scatter σ_{H_2} about the mean fitting trend (right panels) are shown for the size range 200–2000 pc. A non-negligible scatter in the simulated data is present even when there is no scatter between SFR and gas cloud mass.

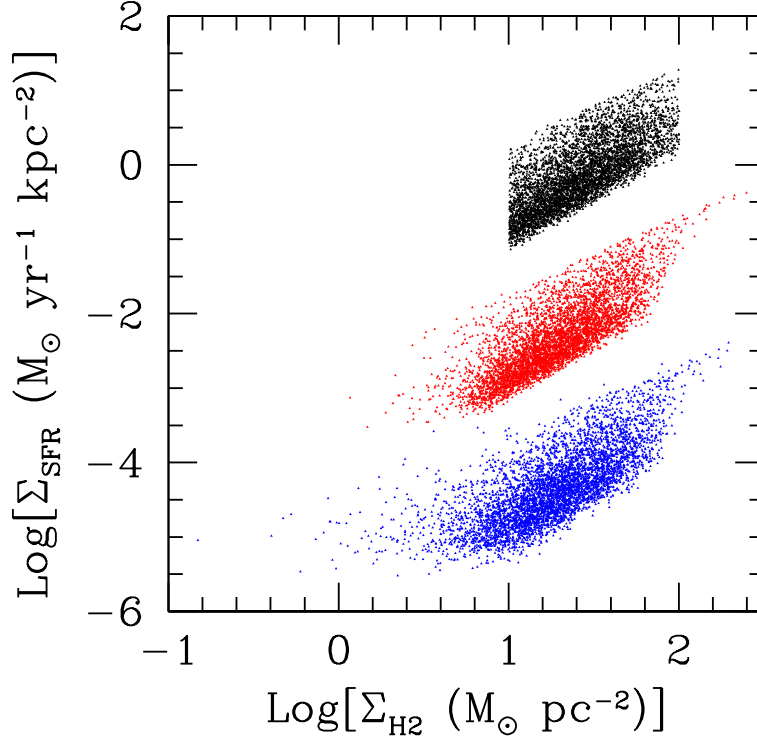


Fig. 6.— The same as Figure 2, for $\beta=1.5$ and 200 pc region size, adding in sources of scatter one at the time. Black points show the distribution of simulated data for our default range of covering factors, exponentially and randomly distributed between 10% and 100%, but without any scatter for the cloud mass-radius correlation and without noise in the measurements of Σ_{H2} . Red points show the distribution of the simulated data with the same assumptions as the black points, plus a 60% scatter in the cloud mass-radius correlation. Blue points show the distribution of the simulated data with the same assumptions as the red points, with in addition a scatter in Σ_{H2} aimed at simulating measurement errors; our Default Model assumes that values of $\Sigma_{\text{H2}} \sim 6.5 \text{ M}_\odot \text{ pc}^{-2}$ are detected at the 3σ level. The addition of both scatters in the cloud mass-radius relation and the Σ_{H2} measurements, especially the latter one, highlights the non-symmetric nature the distributions acquire in logarithmic plots. Once an additional scatter in the SFR-cloud mass relation is added, the distributions of Figure 2 are recovered.

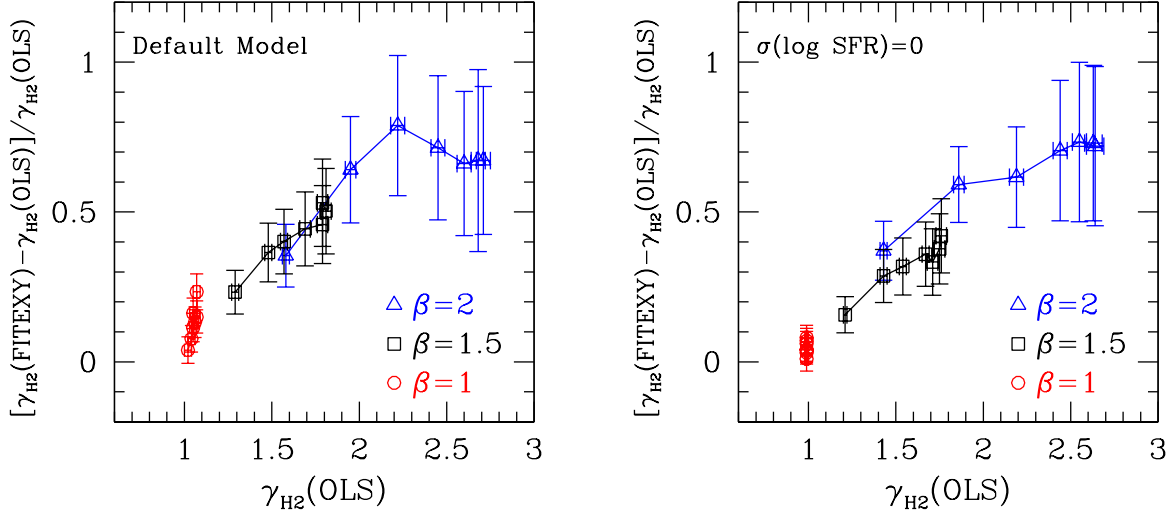


Fig. 7.— A comparison of the best fit slopes γ_{H2} measured by the OLS bi-sector linear fitting method and by the bi-linear regression fitting method (FITEXY). The fractional difference $[\gamma_{H2}(\text{FITEXY}) - \gamma_{H2}(\text{OLS})] / \gamma_{H2}(\text{OLS})$ is plotted as a function of the best fit slope from the OLS fitting method. The Default Model ($\sigma(\log SFR)=0.3$, left panel) and the case of zero scatter between SFR and cloud mass ($\sigma(\log SFR)=0$, right panel; see equation 5) are shown, both for an exponential distribution of cloud covering factors. For each value of β , the difference between the slopes determined with the two methods are shown for our range of region sizes; the sizes move from right to left in the range 200-2,000 pc, in the sense that smaller regions produce steeper slopes with both methods. The bi-linear regression fit always measures values that are larger than those obtained from the OLS bi-sector fit, although in neither case the actual value of β is generally recovered. The slopes obtained via the FITEXY routine show larger error bars than those from the OLS fit, reflecting the use of the data uncertainties in the former fitting algorithm; the FITEXY best fit uncertainties dominate the vertical error bars in the two plots.

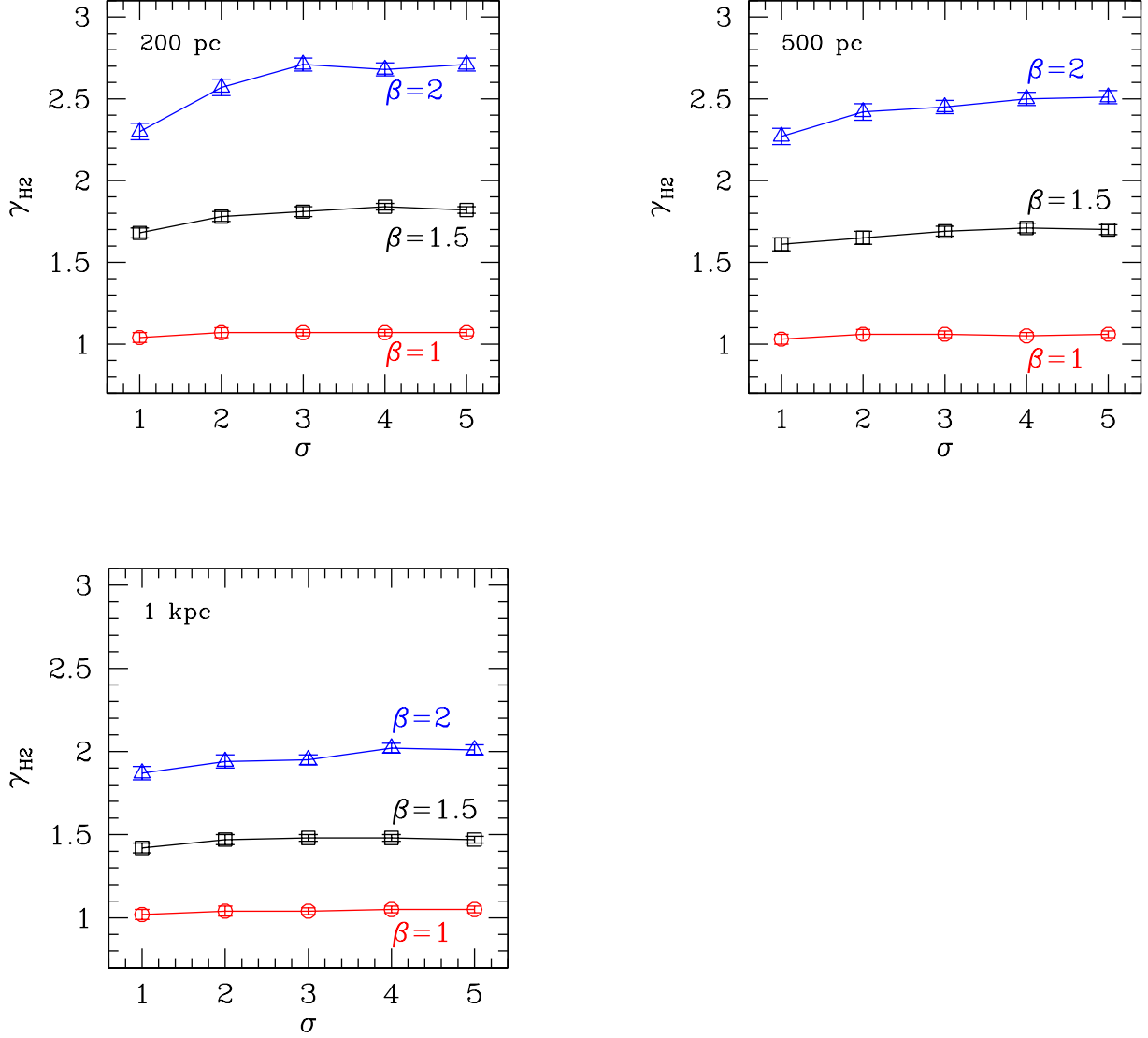


Fig. 8.— The slope γ_{H2} of the Observed SK Law for three representative region sizes (200, 500, 1000 pc), for data thresholds that vary between 1σ and 5σ . The thresholds are varied while keeping the dynamical range of the simulated data unchanged. A modest increase in γ_{H2} for increasing threshold is observed at all region sizes, with the largest variations present for $\beta=2$ ($\delta\gamma_{H2}/\gamma_{H2} \lesssim 15\%$) and the smallest for $\beta=1$ ($\delta\gamma_{H2}/\gamma_{H2} \lesssim 5\%$).

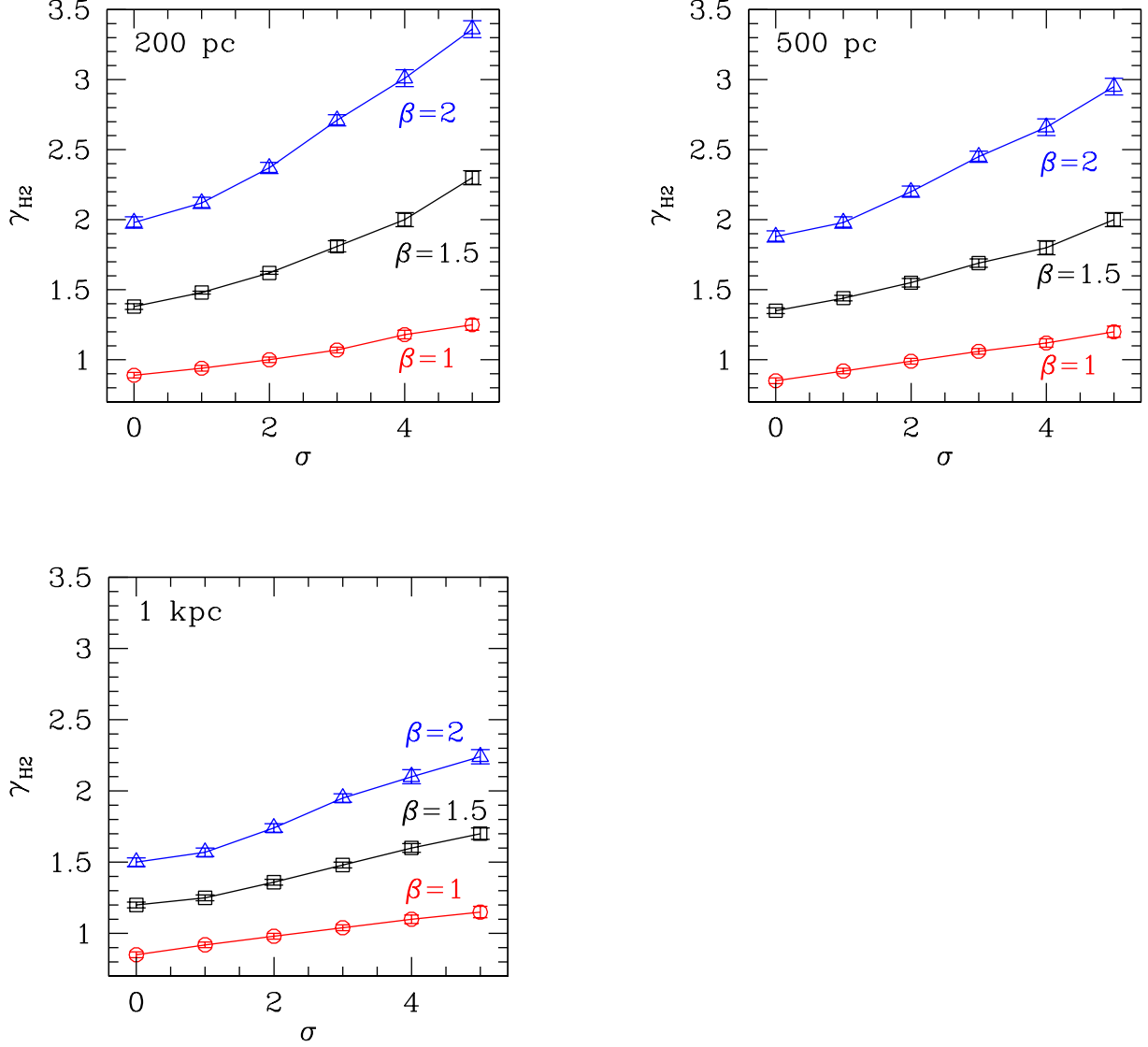


Fig. 9.— The slope γ_{H2} of the Observed SK Law for three representative region sizes (200, 500, 1000 pc), for data thresholds that vary between 0 σ (no threshold; all data included) and 5 σ . The dynamical range of the data varies so that the highest threshold corresponds to the smallest dynamical range for the simulated data. A pronounced increase in γ_{H2} for increasing threshold is observed at all region sizes, unlike Figure 8. As in the previous figure, the largest variations are present for $\beta=2$ ($\delta\gamma_{H2}/\gamma_{H2} \lesssim 45\%$) and the smallest for $\beta=1$ ($\delta\gamma_{H2} \lesssim 20\%$). Note that the vertical scales of Figures 8 and 9 are different.

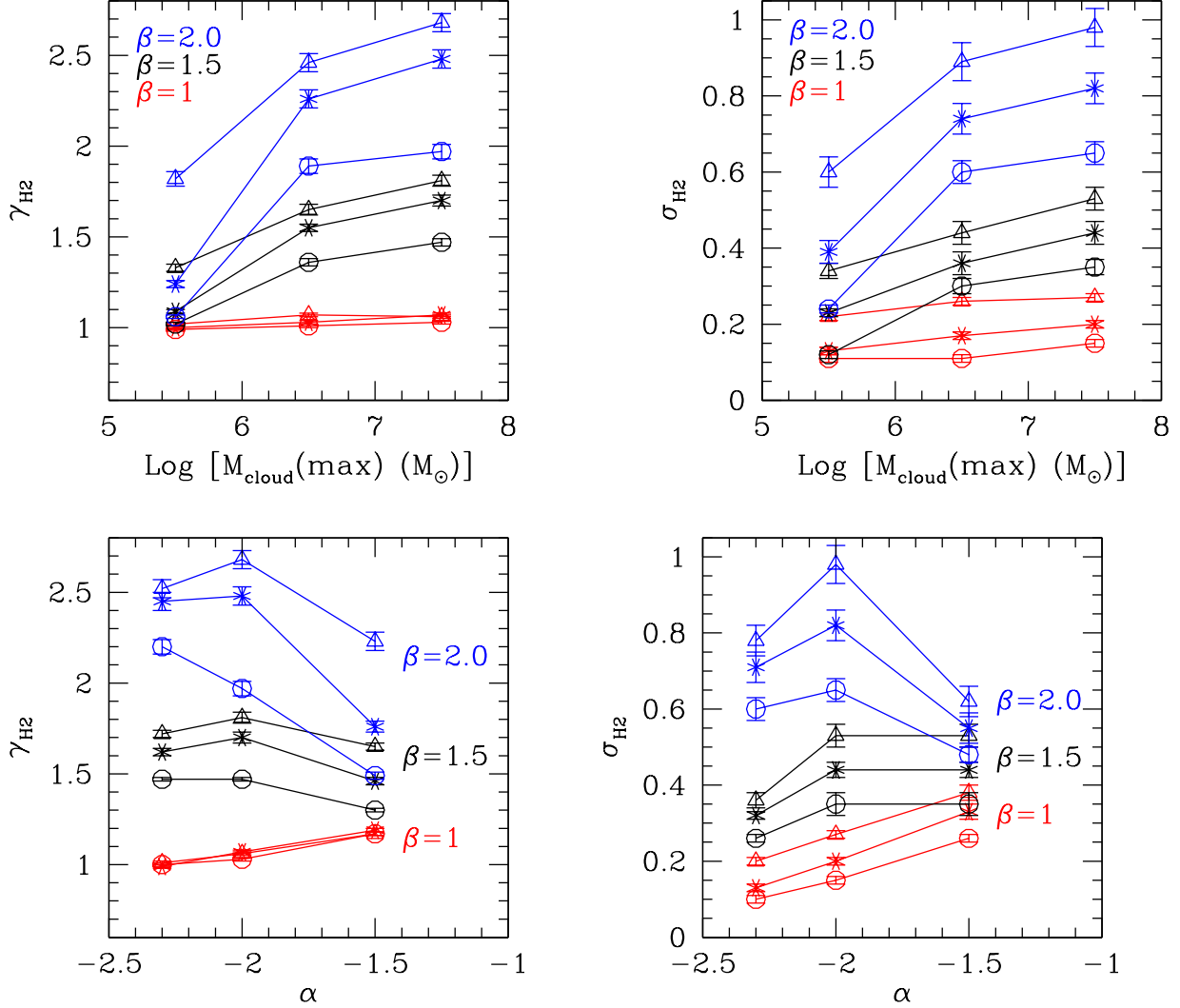


Fig. 10.— The best fit slope γ_{H2} (left panels) and dispersion σ_{H2} about the best fitting line (right panels) of the Observed SK Law as a function of the maximum cloud mass $M_{\text{cloud}}(\text{max})$ (top panels) and of the cloud mass function power law index α (bottom panels; equation 3). The three values for the SFR–cloud mass relation power index (equation 5) are shown: $\beta=1.0$ (red), $\beta=1.5$ (black), and $\beta=2.0$ (blue), for three representative region sizes, 200 pc (triangles), 500 pc (asterisks), and 1 kpc (circles). The decreasing $M_{\text{cloud}}(\text{max})$ pushes γ_{H2} closer to values of unity, which is what is expected when the cloud mass function is fully sampled in each region. A similar overall effect is observed for a flattening cloud mass function (increasing α), when $\beta > 1$.

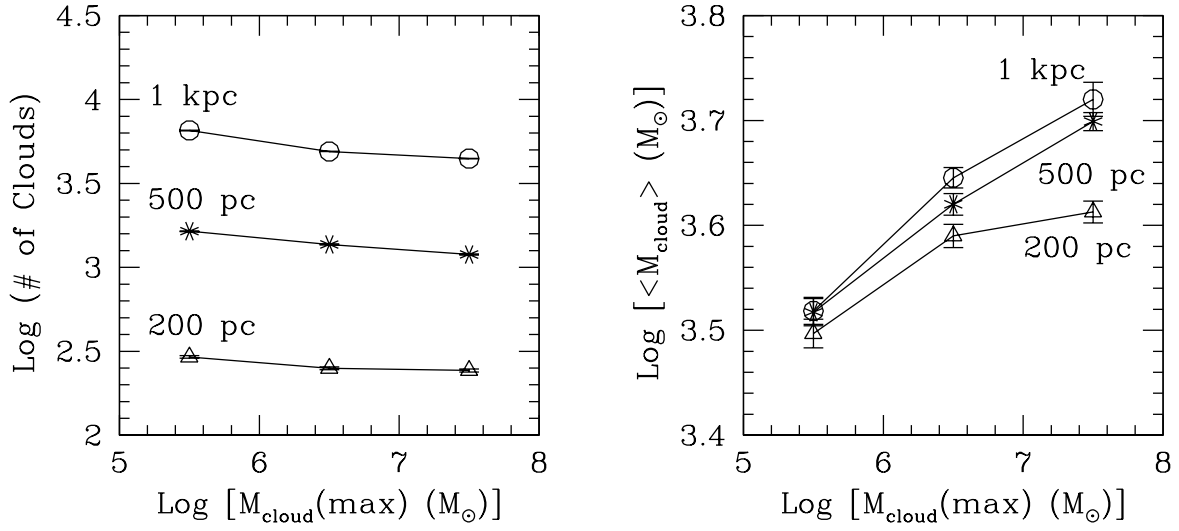


Fig. 11.— The mean number of clouds (left) and the mean cloud mass (right) within a region, as a function of the maximum cloud mass $M_{\text{cloud}}(\text{max})$. Three representative region sizes are shown in each panel: 200 pc (triangles), 500 pc (asterisks), and 1 kpc (circles). Decreasing the maximum cloud mass decreases the mean cloud mass and increases the mean number of clouds in each region.

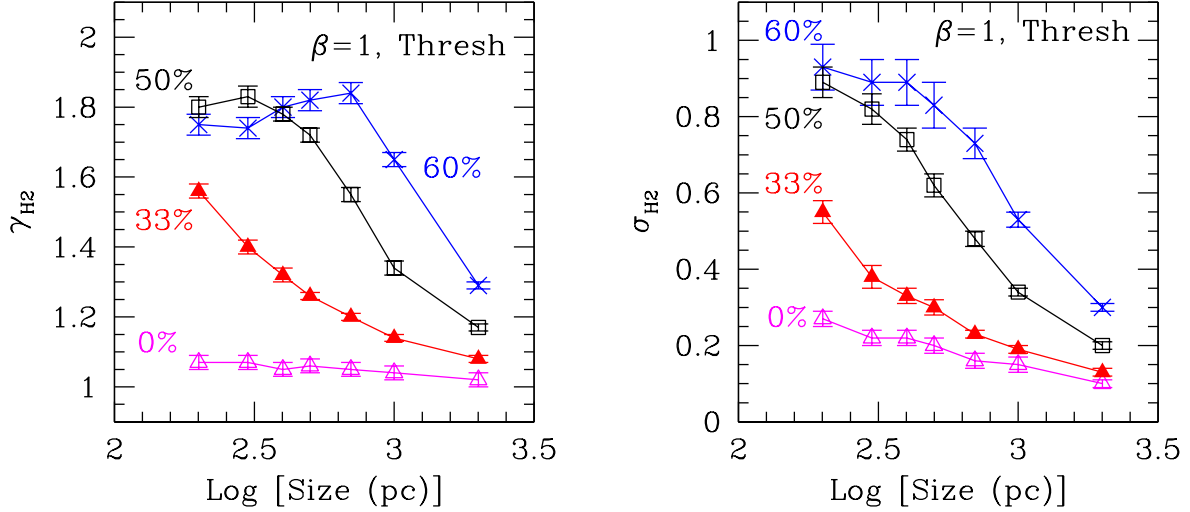


Fig. 12.— The best fit slope γ_{H2} (left panel) and dispersion σ_{H2} about the best fitting line (right panel) of the Observed SK Law (equation 2) as a function of the sampling region’s size, in the range 200-2000 pc. The Default Model is used with the addition of a star formation threshold, an exponential distribution of the cloud covering factor (equation 6), and $\beta=1.0$. The case with no star formation threshold (from Figure 3, bottom panels) is shown for comparison, with label ‘0%’ (magenta empty triangles). The other percentage numbers in the two panels refer to the fraction of the total SFR selectively removed on average from each region, by assigning $SFR=0$ to clouds with mass below a given $M_{cloud}(thr)$. The three cases shown correspond to 1/3 (red filled triangles), 1/2 (black empty squares), and 60% (blue crosses) of the total star formation removed, and threshold masses of $10^{4.3} M_{\odot}$, $10^{5.1} M_{\odot}$, and $10^{5.6} M_{\odot}$, respectively.

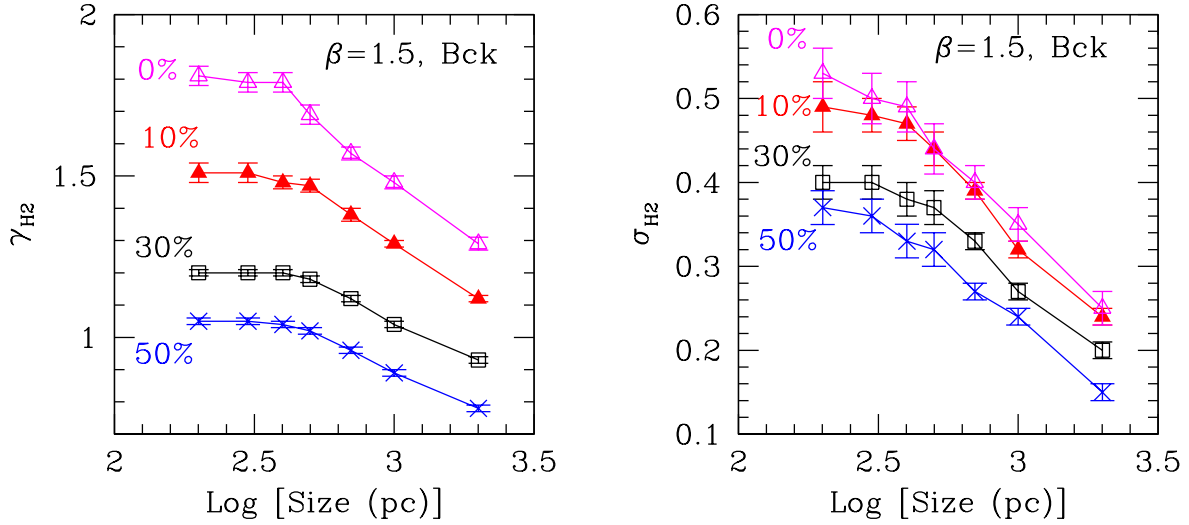


Fig. 13.— The best fit slope γ_{H2} (left panel) and dispersion σ_{H2} about the best fitting line (right panel) of the Observed SK Law (equation 2) as a function of the sampling region’s size, in the range 200-2000 pc. The Default Model with the addition of a uniform background to the star formation, an exponential distribution of the cloud covering factor (equation 6), and $\beta=1.5$ is used. The case with no background added to the star formation (from Figure 3, bottom panels) is shown for comparison, with label ‘0%’ (magenta empty triangles). The percentage numbers in the two panels refer to the fraction of the total SFR that is added into each region as a uniform background, which adds to the region’s measured SFR surface density without contributing to the gas surface density. The three cases in which the added background corresponds to 10% (red filled triangles), 30% (black empty squares), and 50% (blue crosses) of the total SFR are shown.

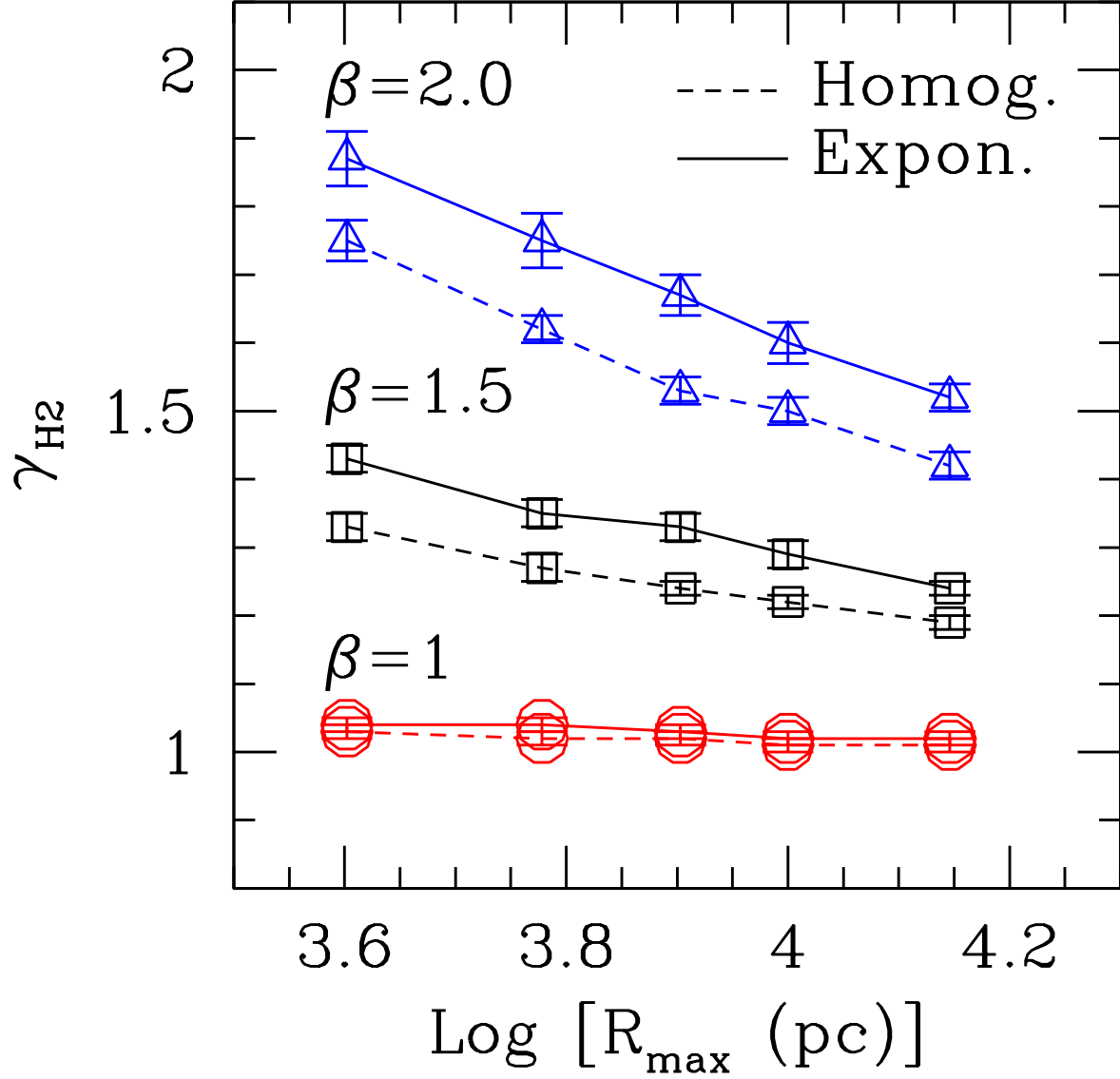


Fig. 14.— The best fit slope γ_{H_2} of the Observed SK Law for the radial profile simulation. Both cases of a uniform (dash lines) and exponential (continuous lines) distribution of cloud covering factors are shown. The Default Model is modified to accommodate the increasing area of the annuli in azimuthally-averaged analyses. The measured values of γ_{H_2} are plotted as a function of the maximum radius, R_{max} , used. The radial step is, in all cases, 200 pc.

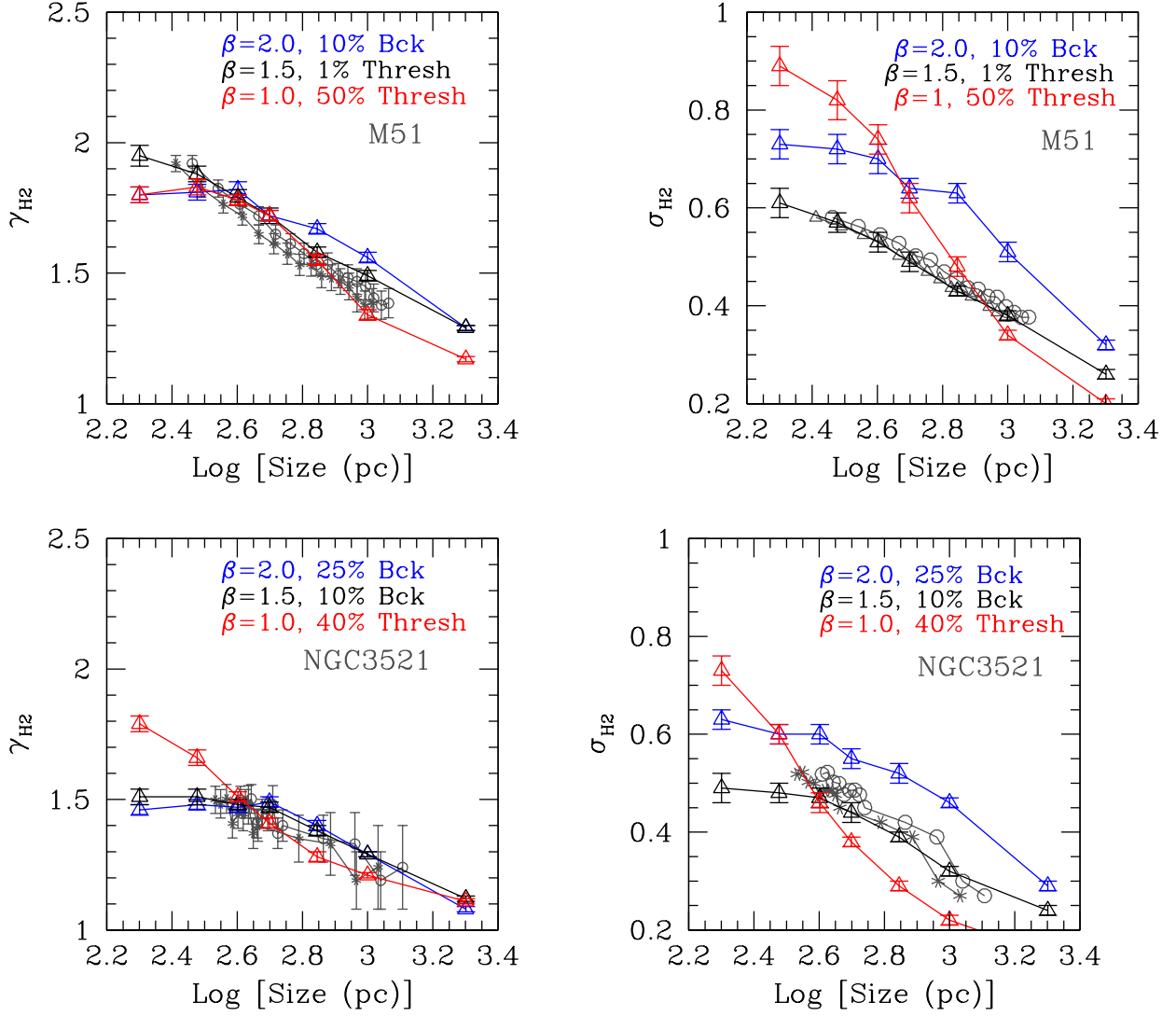


Fig. 15.— The data for γ_{H_2} (left panels) and σ_{H_2} (right panels) for the two galaxies M51a (top panels) and NGC3521 (bottom panels) from Liu et al. (2011) are compared with our simulations, using the Default Model with an exponentially decreasing cloud covering factor. Two extreme values of the inclination are used: 20° – 42° for M51a and 65° – 73° for NGC3521 (grey asterisks and empty circles, respectively). The observed linear sizes are the square root of the de-projected areas in Liu et al. (2011). For each value of β , the simulations that most closely approach the observed γ_{H_2} trends are reported. For $\beta=2.0$ (blue), a uniform background is added to the SFR. For $\beta=1.5$ (black), a small SFR threshold and a uniform background addition to the SFR are required for M51a and NGC3521, respectively. For $\beta=1.0$ (red), the largest SFR threshold compatible with the data is shown for both galaxies.

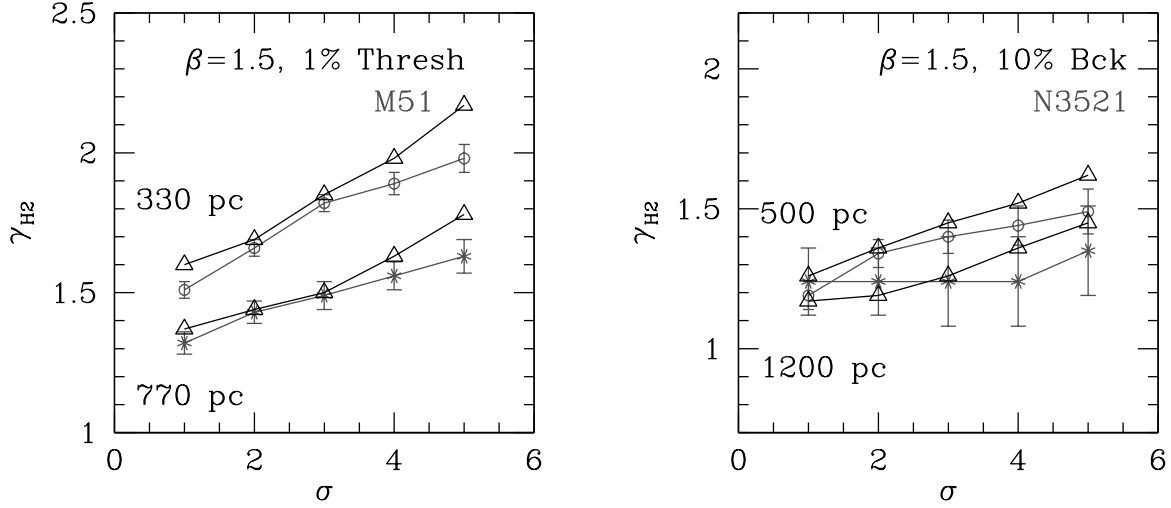


Fig. 16.— Comparison between observed (grey) and model (black) values of γ_{H_2} for M51a (left panel) and NGC3521 (right panel) as a function of the detection limit of the data along Σ_{H_2} , in the range 1σ – 5σ . The increasing limit corresponds to a decrease in the dynamical range of the data along the molecular gas axis. The observational data are from Tables 3 and 4 of Liu et al. (2011), at the two projected sizes of 300 and 700 pc. These correspond to de-projected sizes ~ 330 pc and ~ 770 pc for M51a and ~ 500 pc and $\sim 1,200$ pc for NGC3521. The small size is shown with circles and the large size with asterisks. The Default Model is used with an exponentially decreasing cloud covering factor and $\beta=1.5$. For M51a, the model’s trend is generally consistent with the observational data, although the values of γ_{H_2} are over-predicted at the highest detection limits, due to the increased sensitivity of the fits to the decreasing dynamical range. For NGC3521, there is a general agreement between models and observations within the 1.5σ error of the data, but uncertainties are large for this galaxy. A slightly better agreement is attained for both galaxies between observations and models when a uniform distribution of cloud covering factors is used in the Default Model.